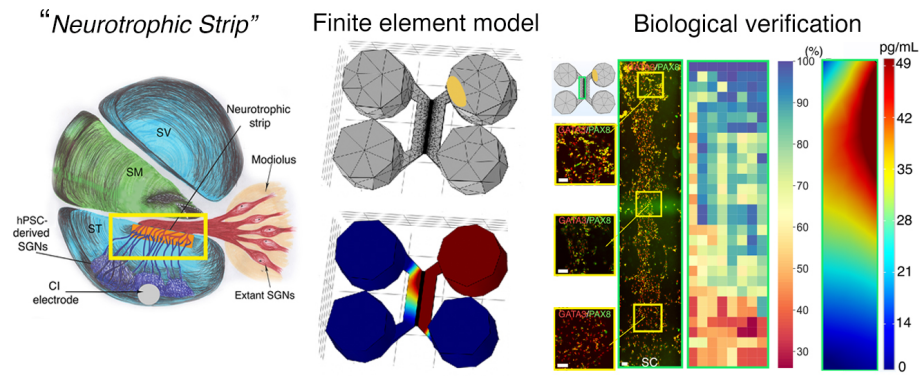


# Graphical Abstract

## Developing the Bioactive Cochlear Implant: Bridging the electrode–neuron gap through neurite guidance

Kevin T. Nella, Benjamin M. Norton, Hsiang-Tsun Chang, Rachel A. Heuer,  
Christian B. Roque, Akihiro J. Matsuoka



# Developing the Bioactive Cochlear Implant: Bridging the electrode–neuron gap through neurite guidance

Kevin T. Nella<sup>a,b</sup>, Benjamin M. Norton<sup>a</sup>, Hsiang-Tsun Chang<sup>a</sup>, Rachel A. Heuer<sup>a</sup>, Christian B. Roque<sup>a</sup>, Akihiro J. Matsuoka<sup>a,c,d,e,\*</sup>

<sup>a</sup>*Department of Otolaryngology–Head and Neck Surgery, Feinberg School of Medicine, Northwestern University, Chicago IL, 60611, USA*

<sup>b</sup>*Department of Mechanical Engineering, Robert R. McCormick School of Engineering and Applied Science, Northwestern University, Evanston, IL., USA*

<sup>c</sup>*Simpson Querrey Institute, Chicago IL, 60611, USA*

<sup>d</sup>*Roxelyn and Richard Pepper Department of Communication Sciences and Disorders, School of Communication, Northwestern University, Evanston, IL., 60210, USA*

<sup>e</sup>*The Hugh Knowles Center for Clinical and Basic Science in Hearing and its Disorders, Evanston, IL. 60210, USA*

---

## Abstract

Although cochlear implant (CI) technology has allowed partial restoration of hearing over the last few decades, persistent challenges remain - including the deciphering of rich acoustic signals into a digital pulse-train signal. Among these challenges, the “electrode–neuron gap” poses the most significant obstacle to advancing past the current plateau in CI performance. Resulting issues include limited performance in noisy environments and a poor ability to decode intonation and music. We propose the development of a “neurotrophic strip”—a biological interface that doubly preserves endogenous spiral ganglion neurons (SGNs) while precisely directing the growth of neurites arising from transplanted human pluripotent stem cell (hPSC)-derived otic neuronal progenitors (ONPS), toward endogenous SGNs. We hypothesized that the Polyhedrin Delivery System (PODS®-human brain-derived neurotrophic factor [BDNF]) could stably

---

\*Corresponding author: Akihiro J. Matsuoka, Department of Otolaryngology–Head and Neck Surgery, Feinberg School of Medicine, Northwestern University, 676 North St. Clair Street Suite 1325, Chicago, IL 60611, USA. E-mail addresses: amatsuok@nm.org, akihiro.matsuoka@northwestern.edu.

Email addresses: kevin.nella@northwestern.edu (Kevin T. Nella), benjamin.norton@northwestern.edu (Benjamin M. Norton), hsiangtsun.chang@gmail.com (Hsiang-Tsun Chang), racheuer@gmail.com (Rachel A. Heuer), christian.b.roq@gmail.com (Christian B. Roque), amatsuok@nm.org (Akihiro J. Matsuoka)

provide an adequate BDNF gradient to hPSC-derived ONPs, thereby simultaneously facilitating otic neuronal differentiation and directional neurite outgrowth. To test this hypothesis, we first devised a finite element model to simulate the *in vitro* BDNF gradient generated by PODS®. For biological verification, we validated the concept of the neurotrophic strip by using a multi-chamber microfluidic device, which mimics the *in vivo* micro-environment more accurately than conventional laboratory plates in terms of volume and concentrations of endogenous/exogenous factors. We were able to generate the optimal BDNF concentration gradient to enable survival, neuronal differentiation toward hPSC-derived SGNs, and directed neurite extension of hPSC-derived SGNs. The technique will allow us to further advance our concept of the “neurotrophic strip” by controlling neurite direction of transplanted hPSC-derived ONPs. This proof-of-concept study provides a step toward the next generation of CI technology.

*Keywords:* human pluripotent stem cells, finite element model, microfluidic device, neurotrophic factor, cochlear implant, neuroelectric interface, stem cell niche, spiral ganglion neurons

*2010 MSC:* 74S05, 62P10, 92C20

---

<sup>1</sup> **1. Introduction**

<sup>2</sup> The cochlear implant (CI), which provides functional restoration in patients  
<sup>3</sup> with sensorineural hearing loss, forms a neuro-electronic interface with the pe-  
<sup>4</sup> ripheral auditory nervous system [1]. CI technology functions by electrically  
<sup>5</sup> stimulating the extant population of auditory neurons (i.e., spiral ganglion neu-  
<sup>6</sup> rons [SGNs]). Although CI technology has allowed partial restoration of hearing  
<sup>7</sup> for this patient population over the last few decades, persistent challenges, in-  
<sup>8</sup> cluding the deciphering of rich acoustic signals into digital pulse-train signals,  
<sup>9</sup> remain. Among these challenges, the “electrode-neuron gap” poses the most  
<sup>10</sup> significant obstacle to advancing past the current plateau in CI performance.  
<sup>11</sup> This phenomenon results in limited performance in noisy environments and poor  
<sup>12</sup> ability to decode intonation and music [2], arguably decreasing quality of life.  
<sup>13</sup> The gap exists between the CI electrode and the target membranes of dendrites  
<sup>14</sup> in surviving endogenous SGNs [3]. It results in the requirement of larger CI  
<sup>15</sup> excitation fields, leading to current spread that excites and therefore disables  
<sup>16</sup> the neighboring electrodes, resulting in fewer information channels to the brain,  
<sup>17</sup> all within discrete time steps [2, 4]. This can develop into a vicious cycle as  
<sup>18</sup> fewer information channels to the brain also prompt the need for larger CI ex-  
<sup>19</sup> citation fields. The length of the gap generally spans hundreds of  $\mu\text{m}$  [5, 6].  
<sup>20</sup> Hahnewald et al. demonstrated *in vitro* that energy needed to elicit a response  
<sup>21</sup> can be reduced by up to 20% by reducing the distance from 40 to zero  $\mu\text{m}$  (by  
<sup>22</sup> growing early postnatal mouse SGN explants on a microelectrode array) [4].

<sup>23</sup> To resolve the electrode-neuron gap *in vivo*, previous work has introduced  
<sup>24</sup> the concept of a bioactive CI (Figure. 1A) [7, 8, 9]. The bioactive CI combines  
<sup>25</sup> the current state-of-the-art CI technology with emerging stem cell-replacement  
<sup>26</sup> therapy in the inner ear. In this scheme, transplanted human pluripotent stem  
<sup>27</sup> cell (hPSC)-derived SGNs bridge the gap between the CI electrode and sur-  
<sup>28</sup> viving endogenous SGNs. Neurotrophin gradients have been shown to guide  
<sup>29</sup> hPSC grafts in spinal cord injury [10], direct growth of endogenous SGNs to-  
<sup>30</sup> ward CI electrodes in the scala tympani [11], and enable transplanted hPSC

31 derived otic neuronal progenitors (ONPs) to grow neurites toward the modiolus  
32 [9]. Although promising, these studies failed to observe adequate directional  
33 neurite outgrowth toward endogenous SGNs (i.e., lack of synaptic connections  
34 between hPSC grafts and endogenous SGNs), presumably preventing significant  
35 improvements in functional recovery of hearing.

36 To confront this issue, we propose the development of a “neurotrophic strip”—a  
37 biological interface that doubly preserves endogenous SGNs while precisely di-  
38 recting the growth of neurites arising from transplanted hPSC-derived ONPs  
39 toward the endogenous SGNs. The highlighted yellow-square area in Figure  
40 1A shows a schematic diagram of this concept. Here, the neurotrophic strip  
41 (shown as an orange rectangle in Figure 1A) stimulates neurite outgrowth from  
42 both the hPSC-derived ONPs and the endogenous SGNs via a neurotrophic fac-  
43 tor gradient [12]. While the concept of a neurotrophin gradient for directional  
44 axonal growth has existed for a few decades, incorporating neurotrophin gradi-  
45 ents into any tissue-engineered scaffold has been extremely challenging due to  
46 the lack of self-sustaining neurotrophin delivery methods—their eventual deple-  
47 tion triggers an accelerated decline in neurite growth and the survival of extant  
48 SGNs [13, 14, 15]. One major contributor is the structurally unstable nature of  
49 neurotrophins, which suffer from fragility and thermo-instability under normal  
50 physiological conditions both *in vitro* and *in vivo*, leading to short half-lives typi-  
51 cally ranging from minutes to hours [16]. This issue can be overcome by utilizing  
52 the polyhedrin delivery system (PODS®)—a crystalline growth factor formu-  
53 lation developed to enable long-term release of growth factors while dampening  
54 degradation rates at the source [17, 18, 19] (Figure 1B). The PODS® technology  
55 has adapted viral machinery to encase a chosen growth factor into polyhedrin  
56 protein cases. The resultant growth factor co-crystals have slow degradation pro-  
57 files under physiological conditions and, therefore, allow the sustained release of  
58 embedded bioactive growth factor protein such as neurotrophins.

59 We reasoned that an bio-engineered scaffolding incorporated with PODS®  
60 technology can establish a neuronal network between transplanted hPSC-derived  
61 ONP grafts and extant SGNs in the inner ear. More specifically, we hypothesized

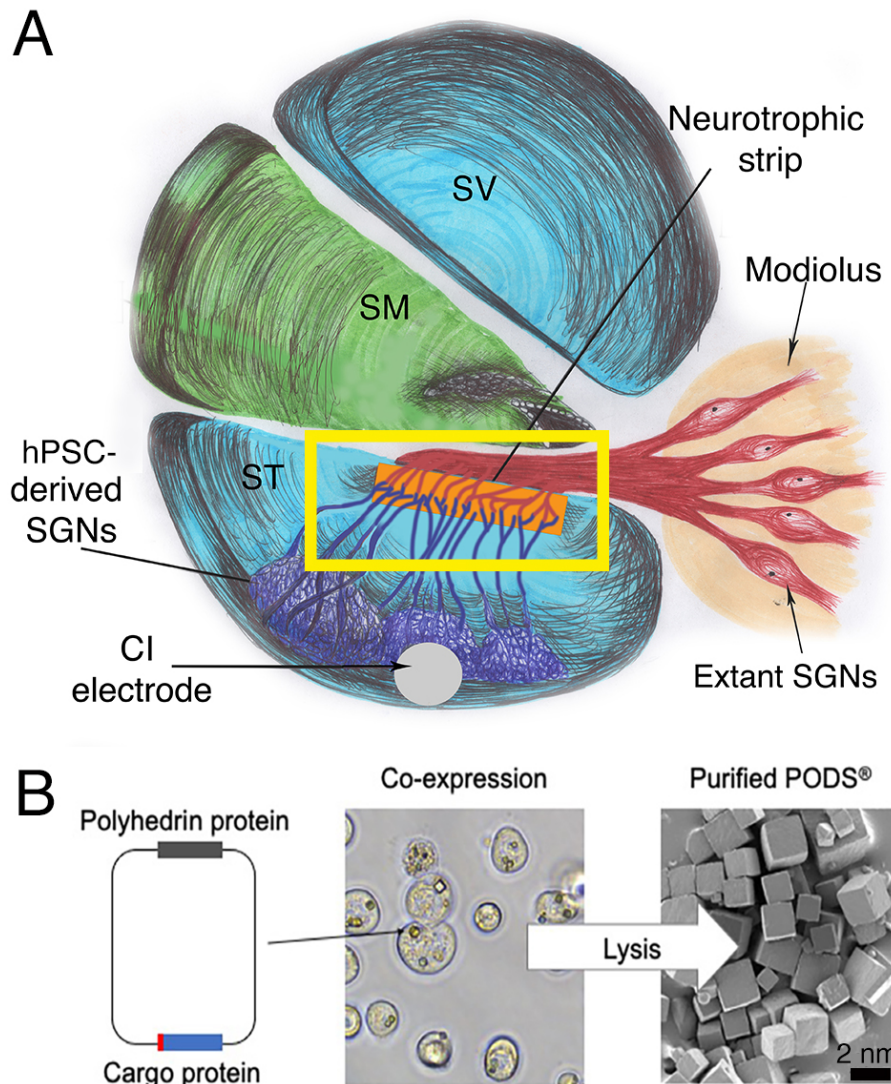


Figure 1: (A): A next-generation bioactive CI and a neurotrophic strip. The neural network in this scheme consists of a CI electrode, transplanted stem cell-derived SGNs, the neurotrophic strip, and extant/endogenous SGNs (red). Note that neuronal connection is largely absent with hair cells (not shown). (B): Polyhedrin Delivery System (PODS)®. PODS® crystals are cubic protein co-crystals produced by Sf9 cells (a clonal isolate of *Spodoptera frugiperda* Sf21 cells [IPLB-Sf21-AE], in which the polyhedrin protein and a second protein are co-expressed). This second protein is termed as the active, or cargo protein (Figure 1B, left). Inside the Sf9 cells, polyhedrin proteins self-assemble into cubic crystals (Figure 1B, center) while the active protein, tagged with a short peptide sequence, binds to the growing polyhedrin crystal. The crystals are extracted and purified by simple cell lysis and washes to remove cell debris (Scanning electron micrograph, Figure 1B, right).

62 that PODS<sup>®</sup>-human neurotrophin system could stably provide and maintain  
63 an adequate neurotrophin gradient to hPSC-derived ONPs, facilitating otic neu-  
64 ronal differentiation and directional neurite outgrowth. To test this hypothesis,  
65 we first devised a finite element model (FEM) to simulate the *in vitro* neu-  
66 rotrophin gradient generated by PODS<sup>®</sup>. In this study, we focus on the role of  
67 BDNF—the most studied of the neurotrophins in the inner ear, and the most  
68 vital for the functional recovery of damaged SGNs [20]. For biological validation  
69 and demonstration we used a multi-chamber microfluidic device, which mimics  
70 the *in vivo* micro-environment of the inner ear more so than conventional lab-  
71 oratory plates in terms of volume and concentrations of endogenous/exogenous  
72 factors [21].

73 **2. Materials and Methods**

74 *2.1. Polyhedrin delivery system*

75 The Polyhedrin Delivery System (PODS<sup>®</sup>-human BDNF [rhBDNF]) (Cell  
76 Guidance Systems, Cambridge, United Kingdom) was used as a self sustaining  
77 source of rhBDNF. PODS<sup>®</sup>-rhBDNF utilizes the polyhedrin protein formed  
78 by *Bombyx mori*, an insect from the moth family *Bombycidae*. A cargo pro-  
79 tein (i.e., rhBDNF) is co-expressed within the polyhedrin crystal and is slowly  
80 released with degradation of the PODS<sup>®</sup> crystals by cell-secreted proteases  
81 (Figure 1B)[9, 18, 22].

82 *2.2. Human pluripotent stem cell culture using dual-compartment microfluidic  
83 device*

84 Human embryonic stem cells (hESCs: H7 and H9, passages number 25–35)  
85 and were obtained from WiCell Research Institute (Madison, Wisconsin, USA).  
86 Human induced pluripotent stem cells (hiPSCs: TC-1133HKK, passage num-  
87 ber 22–35) were generated from human CD34+ cord blood cells using the four  
88 Yamanaka factors at Lonza (Walkersville, Maryland [MD], USA). The hiPSC  
89 cell line (TC-1133HKK) was kindly provided by Healios K.K. (Tokyo, Japan).

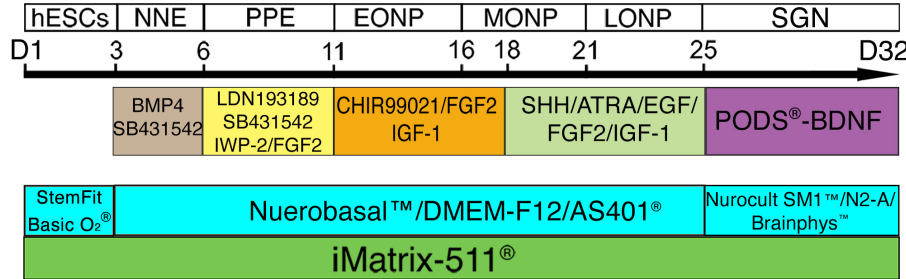


Figure 2: Overview of otic neuronal differentiation protocol for hPSCs. Please see detail in [8, 9, 23, 24] and the Supplemental Data. Each developmental stage is shown at the top, with key treatments shown below. NNE: nonneuronal ectoderm; PPE: preplacodal ectoderm; EONP: early-stage otic neuronal progenitor; MONP: mid-stage otic neuronal progenitor; LONP: late-stage otic neuronal progenitor; BMP4: bone morphogenetic protein 4; SHH: Sonic hedgehog; ATRA: all-trans retinoic acid; EGF: epidermal growth factor; IGF-1: insulin-like growth factor-1; FGF2: fibroblast growth factor 2; N2B27-CDM: chemically defined medium containing N2 and B27 supplements.

90 hPSC-derived ONPs were derived based on our previously established protocol  
 91 (Supplemental Data) [8, 9, 23, 24]. A step-wise series of ligands and growth  
 92 factors was added to a neuronal induction medium to promote hPSC differen-  
 93 tiation toward the late-stage ONP lineage—mitotic progenitor population that  
 94 generates the SGNs. (Figure 2).

95 Microfluidic devices provide a platform for specifically evaluating axonal re-  
 96 generation [25]. Here, multi-chamber microfluidic devices, Xona™ Microfluidics  
 97 XC150 and XC450 (Xona™ Microfluidics, Research Triangle Park, North Car-  
 98 olina, USA), were used for computational calculation and biological validation  
 99 (Figure 3A–B). The Xona™ device allows for neurites to grow toward growth  
 100 factors in the opposite chamber while limiting migration of derived ONP cell  
 101 bodies due to specific dimensions of the device. Additionally, the microchannel  
 102 array between the two chambers mimics the porous bony separation between  
 103 the modiolus (where extant SGNs are localized) and the scala tympani (where  
 104 the biohybrid CI will be implanted). Thus the diffusion profile of the released  
 105 rhBDNF *in vitro* more accurately predicts that of the *in vivo*.

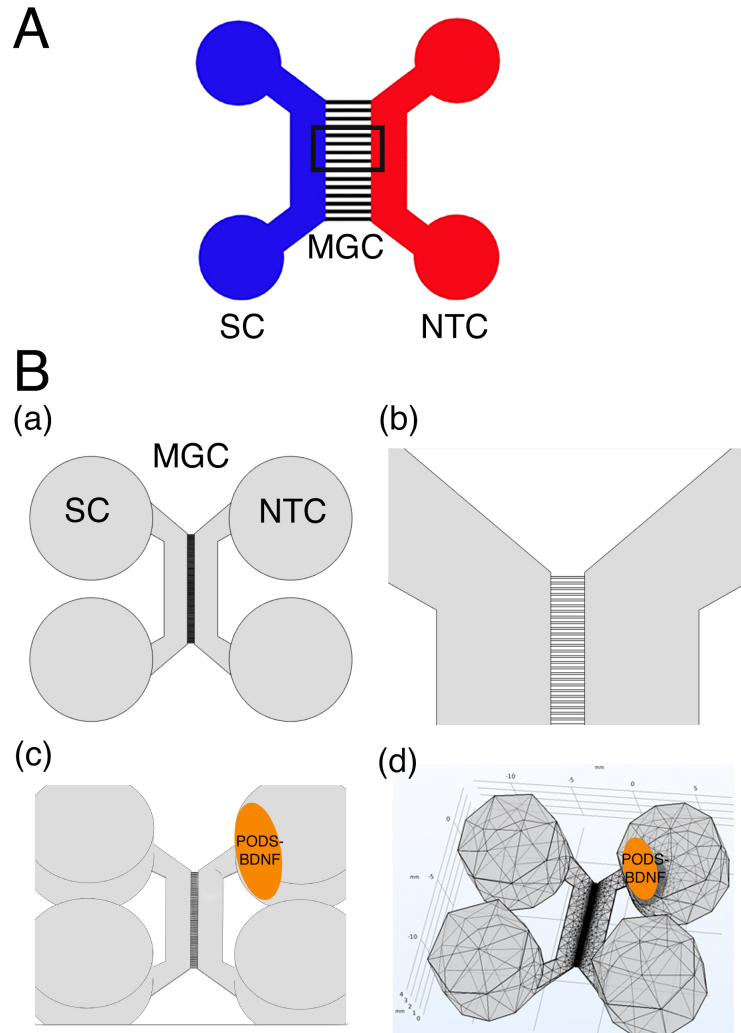


Figure 3: (A): Schematic specification of a Xona™ Microfluidics XC 450. Two main channels (somal compartment (SC) and neurotrophin compartment (NTC)) on either side are connected by a micro-groove channel (MGC) spanning  $450 \mu\text{m}$  with a width of  $10 \mu\text{m}$  (black square). The somal compartment contains hPSC-derived late-stage ONPs (shown in black), while the neurotrophin compartment contains the secreted factors (i.e., BDNF) that are released from PODS®-rhBDNF crystals. (B):(a) Xona™ Microfluidics XC450 device geometry, created at a 1:1 scale with Autodesk Inventor®, in which the diffusion profile of the released BDNF was modeled and tested. (b) Detail of the microchannels joining the two compartments of the Xona™ Microfluidics XC450. (c) Xona™ Microfluidics XC450 device showing the optimized area and geometry to localize PODS® containing rhBDNF (yellow ellipsoid area). (d): Mesh geometry of the Xona™ XC450 generated with Autodesk Inventor, depicting the localized volume of PODS®-rhBDNF ( $1 \mu\text{L}$ ) as an ellipsoid disk.

106 The devices were washed and coated with poly-L-ornithine (PLO, 20  $\mu$ g/mL  
107 in H<sub>2</sub>O, Sigma-Aldrich, St. Louis, Missouri [MO], USA) and recombinant  
108 laminin-511 (iMatrix-511, 0.5 mg/mL, Nacalai USA, San Diego, California [CA],  
109 USA) according to the manufacturer-outlined protocol. Next, approximately  
110 1.75 x 10<sup>5</sup> cells (in 20  $\mu$ L of media) were added through the top and bottom left  
111 wells to the somal compartment (i.e., the total amount of 3.5 x 10<sup>5</sup> hPSC-derived  
112 ONPs were added).

113 PODS®-rhBDNF were placed in the top right well of the neurotrophin com-  
114 partment (Figure 3A–B) to generate a BDNF concentration gradient to promote  
115 directional neurite growth. hPSC-derived ONPs were cultured for 7 days in the  
116 Xona™ device to induce otic neuronal differentiation. Note that due to our  
117 use of the microfluidic device, high-density cell cultures were induced to facil-  
118 itate molecular studies as well as the generation of a more biologically relevant  
119 neuronal phenotype (i.e., otic lineage) [25]. Media was topped off daily after  
120 imaging (from 20-40  $\mu$ L per well).

121 *2.3. Three-dimensional finite element model*

122 We used finite element analysis (FEA) to simulate the BDNF concentration  
123 gradient in a multi-chamber microfluidic device during release and subsequent  
124 degradation. FEA is a computational numerical technique, which approximates  
125 mathematical solutions to partial differential equations (PDEs) that appropri-  
126 ately simulate complex real-world problems. In this study, the finite element  
127 model allowed us to predict the concentration gradient with respect to time in  
128 the multi-chamber microfluidic device, depending on the number of PODS®-  
129 rhBDNF introduced into the system. To solve the finite element model, we used  
130 COMSOL® Multiphysics (version 5.6 [released on November 11, 2020], COM-  
131 SOL, Inc., Burlington, Massachusetts [MA], USA), which is a finite element  
132 method solution tool for engineering and scientific research computations. We  
133 used sustained-release kinetics for PODS®-rhBDNF determined from an ELISA  
134 study (see next subsection) as well as data from a previous study from our group  
135 [9]. Device geometry was generated at a 1:1 scale using Autodesk® Inventor

136 2019.0.2 (Autodesk, Mill Valley, CA, USA) (Figure 3B). The computational  
137 analysis was implemented on a high-performance desktop computer platform  
138 equipped with a CPU (AMD Ryzen Threadripper 3990X 64-Core, 128-Thread  
139 @ 4.3 GHz) with 64 GB RAM, and two GPU cards (NVIDIA GeForce RTX  
140 3080Ti,12GB 384-bit GFF6X Graphics card).

141 *2.4. Enzyme-linked immunosorbent assay for brain-derived neurotrophic factor*

142 In order to determine the release and degradation kinetics of PODS<sup>®</sup>-  
143 rhBDNF, an experiment measuring concentrations at sequential time points was  
144 performed. To measure the concentration of rhBDNF secreted from PODS<sup>®</sup>-  
145 rhBDNF crystals, the culture media from both a control and an experimental  
146 condition were collected at each time point and immediately stored at -80°C  
147 before running an enzyme-linked immunosorbent assay (ELISA) after the final  
148 collection. The same method was applied to measure the degradation kinetics  
149 of rhBDNF protein with a carrier protein (Bovine Serum Albumin [BSA])  
150 (#248-BDB-050, R&D Systems, Minneapolis, Minnesota, USA). Experimen-  
151 tal conditions were culture media enriched with 10% fetal bovine serum (FBS)  
152 (Thermo Fisher Scientific, Waltham, MA, USA). All samples were quantified  
153 with a BDNF ELISA kit (# BGK23560; PeproTech, Rocky Hill, New Jersey,  
154 USA), and the results were analyzed with a Synergy HTX Multi-Mode Reader  
155 (BioTek, Winooski, Vermont, USA) at a 450 nm wavelength, as instructed by  
156 the manufacturer. Release and degradation kinetics were then calculated using  
157 MATLAB Curve Fitting Toolbox (MathWorks, Natick, CA, USA).

158 *2.5. Sodium dodecyl sulphate-polyacrylamide gel electrophoresis*

159 Sodium dodecyl-sulfate polyacrylamide gel electrophoresis (SDS-PAGE) is  
160 commonly used as a method to separate proteins with molecular masses be-  
161 tween 5 and 250 kDa [26], a range of which is suitable for detecting human  
162 BDNF protein (molecular weight [MW]: 14kDa [27]) and polyhedrin (MW: ~29  
163 kDa [22]). In this study, SDS-PAGE was used to assess the molar ratio of  
164 BDNF to polyhedrin in each sample. Briefly, each protein sample was diluted

165 in deionized water and mixed with 6x Laemmli sample buffer (Bio-Rad Labora-  
166 tories, Inc., Des Plaines, Illinois [IL], USA) containing 2-mercaptoethanol and  
167 heated at 100°C for 5 to 20 minutes. Samples were then loaded into precast  
168 Mini-PROTEAN TGX 4-15% polyacrylamide mini-gels (Bio-Rad Laboratories,  
169 Inc., Des Plaines, IL, USA). Then, 5 mL of Precision Plus Protein Kaleido-  
170 scope Prestained Protein Standards (Bio-Rad Laboratories, Inc., Des Plaines,  
171 IL, USA) were loaded in each gel run. Electrophoresis was performed at room  
172 temperature for approximately 90 minutes using a constant voltage (100V) in  
173 1x solution of Tris-Glycine-SDS electrophoresis buffer (Bio-Rad Laboratories,  
174 Inc., Des Plaines, IL, USA) until the dye front reached the end of the 60 mm  
175 gel. After electrophoresis, the mini-gels were rinsed with deionized water 3  
176 times for 5 minutes and were subsequently incubated in SimplyBlue™ SafeStain  
177 (ThermoFisher Scientific, Waltham, MA, USA) for one hour at room temper-  
178 ature with gently agitation. Images obtained from gels were analyzed using  
179 ImageJ 1.53g (December 4, 2020, the National Institutes of Health, Bethesda,  
180 MD, USA [28]). The calculated molar ratio was applied to the COMSOL®  
181 Multiphysics model to accurately predict the amount of rhBDNF released from  
182 PODS®-rhBDNF. SDS-PAGE was performed according to the manufacturer's  
183 technical guide (Bio-Rad Laboratories, Inc., Des Plaines, IL, USA).

184 *2.6. Western Blot*

185 The identity of the BDNF protein detected by SDS PAGE was verified by  
186 western blot (Bio-Rad Laboratories, Inc., Des Plaines, IL, USA). Briefly, the  
187 polyvinylidene difluoride (PVDF) membrane was prepared in methanol for 30  
188 seconds before soaking in 1x Tris-Glycine-Methanol transfer buffer for 10 min-  
189utes. Wet transfer was performed at 4°C for approximately 60 minutes using a  
190 constant voltage (100V) in 1X solution of Tris-Glycine-Methanol transfer buffer.  
191 After transfer, the membrane was briefly rinsed with 1X Tris-buffered saline  
192 Tween-20 (TBST) and was subsequently blocked in 5% BSA in TBST for 24  
193 hours at 4°C with gentle agitation. The membrane was then rinsed with 1x  
194 TBST before incubating in BDNF polyclonal antibody (ThermoFisher Scien-

tific, Waltham, MA, USA) diluted to 1:1500 in 1% BSA in TBST for 24 hours at 4°C with gentle agitation. Following incubation, the membrane was rinsed in 1x TBST 5 times for 5 minutes to remove unbound primary antibody. Then, the membrane was incubated in Goat anti-Rabbit IgG (H+L) horseradish peroxidase (HRP) conjugated secondary antibody (ThermoFisher Scientific, Waltham, MA, USA) diluted to 1:5000 in 1% BSA in TBST for one hour at room temperature with gentle agitation. Following incubation, the membrane was rinsed in 1x TBST 5 times for 5 minutes to remove unbound secondary antibody. For sensitive detection, the membrane was treated with Pierce™ ECL Western Blotting Substrate (ThermoFisher Scientific, Waltham, MA, USA), and visualized using an Azure 600 Digital Imager (Azure Biosystems, Dublin, CA, USA). Electrophoresis buffer for sample condition and run condition was summarized in Supplementary Table S1.

*2.7. Immunocytochemistry and image acquisition*

Glass coverslips (Corning Inc., Corning, New York, USA) were coated with poly-d-lysine (PDL) (#A3890401, ThermoFisher Scientific, Waltham, MA, USA) and poly-ornithine (PLO) (# A-004-C, MilliporeSigma, St. Louis, MO, USA) affixed to a somal compartment as per the manufacturer's instructions. A total of 100,000 dissociated hPSC-derived ONPs were plated onto a somal compartment of the device. On Day 7, 4% (w/v) paraformaldehyde (PFA) (ThermoFisher Scientific, Waltham, MA, USA) was added to the compartments for 20 minutes to fix the cells. ICC was used to stain for GATA3, PAX8, and beta-III tubulin. These three proteins have shown to appropriately characterize ONPs in our previous studies [8, 9, 24]. Following PBS wash, cultures were blocked with 5% BSA at room temperature for 1 hour. Cultures were then incubated overnight at 4°C on a shaker plate in primary antibody solution using Rabbit anti-Beta-III-Tubulin (1:100, Abcam, Cambridge, MA, USA), Goat anti-PAX8 (1:500, Abcam, Cambridge, MA, USA), and Mouse anti-GATA3 (1:500, R&D Systems, Minneapolis, MN, USA). Following PBS washes, cultures were incubated at room temperature for 90 minutes on a shaker plate in sec-

225      ondary antibody solution composed of Alexafluor647 anti-Rabbit (1:1000, Ther-  
226      moFisher Scientific, St. Louis, MO, USA), Alexafluor488 anti-Goat (1:1000,  
227      ThermoFisher Scientific, St. Louis, MO, USA), and Alexafluor594 anti-Mouse  
228      (1:1000, ThermoFisher Scientific, St. Louis, MO, USA) in 1% BSA. Following  
229      PBS -/- washes, cultures were incubated with DAPI for 20 minutes (300 nM,  
230      ThermoFisher Scientific, St. Louis, MO, USA). Secondary antibody controls  
231      were performed each time multiple primary antibodies were used [29]. Label-  
232      ing controls (detection controls) were performed for a sample from each batch  
233      of hPSC culture [29]. See Supplementary Figure S1 for exemplary figures for  
234      these control conditions. Results were imaged using a Nikon Ti2 Widefield  
235      Laser Microscope System (Nikon, Tokyo, Japan). Phase-contrast images were  
236      captured on a Nikon Eclipse TE2000-U inverted microscope (Nikon, Tokyo,  
237      Japan). All fluorescence images were acquired on a Zeiss LSM 510 META laser-  
238      scanning confocal microscope (Carl Zeiss, Oberkochen, Germany), a Nikon Ti2  
239      laser laser-scanning confocal microscope (Nikon, Tokyo, Japan), or a Leica SP5  
240      laser-scanning confocal microscope (Leica, Welzlar, Germany). Observers were  
241      blinded to the conditions during imaging and tracing. In general, the images  
242      were processed with a Image J ver. 1.53j or Matlab R2020b. Further detail on  
243      image acquisition and quantification of fluorescent-positive cells can be found  
244      in the Supplemental Data.

245      *2.8. Preferred cell orientation analysis*

246      Collective cell migration, where cells organized in a tightly connected fashion  
247      migrate as cohesive structures, is a critical biological process to highlight the  
248      neurotrophin diffusion gradient profile [30]. To evaluate this process, time-lapse  
249      acquisition of images of the Xona™ device was performed using an inverted mi-  
250      croscope (Nikon Eclipse TS100, Tokyo, Japan) at Day 1, 3, 5, and 7. Due to the  
251      high cell density required for hPSC-ONPs to survive in the somal compartment  
252      of the Xona™ device, images were not amenable to manual analysis in most of  
253      the cases. To circumvent this problem, we performed a series of image pre-  
254      processings that are mainly based on modified binarization-based extraction of

aliment score methods with some modifications [31]. We used MATLAB Image Processing Toolbox R2020b (version 9.9.0.1495850, September 30th, 2020, Mathworks, Natick, MA) for analysis. Please see Supplementary Figure S2 for further detail. The analysis of directional data in general represents a particular challenge: there is no reason to designate any particular point on the circle as zero, as it is somewhat arbitrary depending on where one sets a coordinate [32, 33]. In this study, we used polar coordinates to determine the directionality of preferred cell orientation. For this analysis, we again used MATLAB Image Processing Toolbox R2020b. See detailed discussion on how we determined the preferred cell orientation in Supplementary Figure S3.

*2.9. Neurite alignment vector assay, neurite growth assay and cell migration assay*

The microfluidic device allowed us to culture hPSC-derived ONPs in a polarized manner and to directly isolate/analyze neurites. To evaluate the neurite projection into the neurotrophin compartment by derived otic neurons cultured in the somal compartment, we performed a neurite alignment vector assay. We also evaluated the length of neurites that grew from hPSC-derived ONPs. For these purposes, hPSC-derived ONPs were cultured in a Xona™ XC450 for seven days and then immunostained with *beta*-III tubulin and DAPI. We used two ImageJ plug-in toolkits, NeuriteTracer and NeuronJ, to assess neurite alignment and neurite growth [34, 35]. Due to the bipolar nature of hPSC-derived ONPs/SGNs, we measured the two longest neurites from the cells [24, 36]. Please see Supplementary Figure S4 for detailed description of this analysis. We used hPSC-derived ONPs cultured with 800,000 PODS®-rhBDNF as a positive control. The number 800,000 was chosen based on our FEM in that there was no neurotrophin gradient in a somal compartment. As a negative control, we used 20 ng/mL of recombinant human BDNF. To evaluate cell migration across a microgroove channel, we performed cell migration analysis. We manually counted the number of ONPs that migrated from the somal compartment into the microchannels, as well as the neurotrophin compartment.

285     *2.10. Statistical analysis*

286     When appropriate, and as indicated in each figure, statistical analysis was  
287     performed. Experimental values are typically expressed as mean and standard  
288     error (SE). The majority of the statistical analyses were performed with Python  
289     3.9.6. (Python Software Foundation, Wilmington, Delaware, USA). The follow-  
290     ing libraries were used for the statistical analysis: Scipy, Numpy, Matplotlib,  
291     and Seaborn [37, 38, 39]. Normal distributions were assumed unless mentioned  
292     otherwise. *P* values smaller than 0.05 were considered statistically significant.  
293     For circular statistics, we derived the sample mean vector and its polar coor-  
294     dinate. Mean and confidence intervals were calculated. We chose confidence  
295     coefficient, *Q*, e.g. *Q* = 0.95. To analyze the axial nature of data, especially to  
296     compute the mean vector angle, we doubled each angle and reduced the mul-  
297     tiples modulo 360°. Please see detailed discussion in Supplementary Figure S3  
298     and S5. The Rayleigh test of uniformity and V-test were performed to deter-  
299     mine whether the samples differ significantly from randomness (i.e., where there  
300     is statistical evidence of directionality). One-sample test for the mean angle was  
301     performed to test whether the population mean angle is statistically different  
302     from the given angle. In all of our circular statistics, von Mises distribution was  
303     assumed and also verified. Circular statistics were performed using CircStat: A  
304     MATLAB Toolbox [33, 40]. Please see detailed description of circular statistics  
305     in Supplementary Figure S3 and S5. Experiments were done in three biological  
306     replicates unless otherwise specified in Figure captions.

307     **3. Results**

308     The appropriate number of PODS®-rhBDNF crystals to induce an effective  
309     neurotrophin gradient for otic neuronal differentiation and neurite outgrowth  
310     was calculated using a three-dimensional FEA that predicts the concentration  
311     profile of BDNF formed through the gradual release and diffusion of BDNF  
312     from PODS®-rhBDNF. We first empirically tested two available microchannel  
313     lengths—(i.e., Xona™-XC150 [150 μm] and Xona™-XC450 [450 μm]). This was

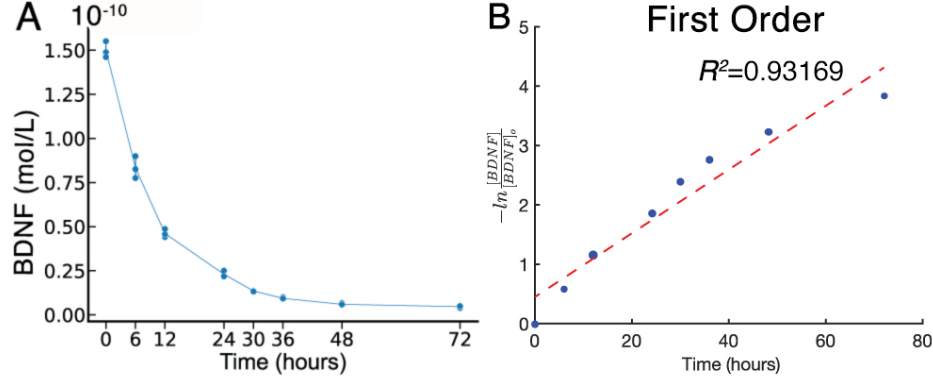


Figure 4: Chemical kinetics of Brain Derived Neurotrophic Factor (BDNF). (A): Concentration of rhBDNF in solution over 72 hours after initial application. (B):  $\frac{1}{[BDNF]}$  data fit to first order curve. Please see other curve fit data in Supplemental Figure 1. Red line: fitted line, blue dots: individual data point.  $k_2$  is defined as slope of fitted curve.

314 done initially because mass (i.e., BDNF) transport from the neurotrophin com-  
 315 partment through the micro-groove channels into the somal compartment is an  
 316 important factor in generating the concentration gradient *via* diffusion mixing.  
 317 We determined that the Xona™ Microfluidics XC450 was more appropriate for  
 318 this study as the XC-150's micro-groove channels were not long enough to gener-  
 319 ate the appropriate concentration gradient throughout the somal compartment.  
 320 This feature is relevant to human inner ear because the micro-groove channels in  
 321 the Xona device simulates the presence of the osseous spiral lamina and modi-  
 322 olus between the scala tympani and SGNs [41, 42]. Following device selection,  
 323 we generated a three-dimensional geometry mesh of the Xona™ Microfluidics  
 324 XC450 for the FEA (Figure 3B(d)). Please also see Supplementary Figure S6  
 325 for detailed measurements of the mesh.

We then quantified the chemical kinetics of the degradation of PODS®-rhBDNF followed by the release and eventual degradation of the rhBDNF by ELISA testing (Figure 4) to establish the parameters for the FEA. Here, two consecutive chemical reactions occur: 1) the release of rhBDNF through degra-  
 dation of PODS® crystals, and 2) the degradation of rhBDNF toward the degra-

dation product (Equation (1)).



326 where  $DP$  is the degradation product of the released rhBDNF, and  $k_1$  and  $k_2$   
327 are the rate constants ( $\frac{1}{hour}$ ) for their respective reactions.

328 Degradation kinetics for rhBDNF was collected while monitoring rhBDNF  
329 concentration after introducing a predefined amount of rhBDNF into a single  
330 well of solution. The data obtained throughout the first 72 hours indicate an  
331 exponential decay, suggesting first order kinetics (Figure 4). To confirm this  
332 notion, we performed a linear and nonlinear least square analysis of the kinetic  
333 data with the MATLAB Curve Fitting Toolbox. We found that the correspond-  
334 ing  $R^2$  was 0.93169 for the first order curve-fit, confirming that the degradation  
335 kinetics was indeed first order (See further detail in Supplementary Figure S7).  
336 Data for the entire reaction were collected while monitoring rhBDNF concen-  
337 tration over time after placing a predefined amount of PODS®-rhBDNF into  
338 a single well of solution. The rhBDNF concentration over time data collected  
339 for the PODS degradation and the release and degradation of rhBDNF seemed  
340 to fit the curve of the Equation 2, which describes the concentration of the  
341 intermediate product of two consecutive first order reactions. We successfully  
342 fit the data to the curve and determined  $k_1$  after plugging in  $k_2$ . The chang-  
343 ing concentration of rhBDNF (the intermediate product) can be expressed as  
344 follows:

$$C_{rhBDNF} = C_{PODS} \cdot k_1 \cdot \left( \frac{e^{-k_1 \cdot t}}{k_2 - k_1} + \frac{e^{-k_2 \cdot t}}{k_1 - k_2} \right) \quad (2)$$

345 where  $C_{rhBDNF}$  is the concentration of rhBDNF and  $C_{PODS}$  is the concentra-  
346 tion of PODS® [43].

347 The rate constant  $k_2 = 0.0679$  ( $\frac{1}{hour}$ ) was calculated by fitting data (obtained  
348 through the experiment solely monitoring rhBDNF degradation) to a first-order  
349 reaction curve to identify the best fit.  $k_2$  was then plugged into Equation (2) to  
350 determine  $k_1$ , which was 0.00686 ( $\frac{1}{hour}$ ). PODS®-rhBDNF release/degradation  
351 data are then curve fitted to this equation to approximate  $k_1$ . The resulting

<sup>352</sup> chemical gradient can be solved using Fick's second Law of diffusion by applying  
<sup>353</sup> the appropriate boundary and initial conditions as follow:

$$\frac{\partial C}{\partial t} = \nabla \cdot (\nabla C \cdot D) - k_2 \cdot C \quad (3)$$

Boundary conditions:

$$\delta C \Big|_{walls} = 0 \quad (4)$$

<sup>354</sup> and

$$\delta C \Big|_{PODS} = k_1 \cdot PODS_0 \cdot e^{-k_1 \cdot t} \quad (5)$$

Initial conditions:

$$C \Big|_{t=0} = 0 \quad (6)$$

<sup>355</sup> where  $C$  is the concentration of rhBDNF,  $D$  is diffusivity of rhBDNF (6.76  
<sup>356</sup>  $\frac{mm^2}{day}$  [44]),  $-k_2 \cdot C$  is the sink term corresponding to the degradation and cell-  
<sup>357</sup> utilization of the rhBDNF.  $PODS_0$  is the initial concentration of the cargo  
<sup>358</sup> protein (i.e., BDNF) within the PODS® crystals. The first boundary condition  
<sup>359</sup> (Equation 4) shows that the concentrations of rhBDNF at the walls of the  
<sup>360</sup> microfluidic device are fixed at 0. The second boundary condition (Equation 5)  
<sup>361</sup> represents the exponential nature of decay of the PODS®. Note that both of  
<sup>362</sup> them are Neumann boundary conditions.

<sup>363</sup> As mentioned, we used the first-order fitted data from our ELISA experi-  
<sup>364</sup> ment and then determined the values of the  $k_{1,2}$  coefficients, which were then  
<sup>365</sup> applied to the diffusion equation. The finite element model was then computed  
<sup>366</sup> for different PODS®-rhBDNF concentrations and time intervals to optimize  
<sup>367</sup> the rhBDNF concentration gradient for hPSC-derived ONP differentiation into  
<sup>368</sup> SGNs and directed neurite extension. Figure 5 shows FEA-computed rhBDNF  
<sup>369</sup> concentration gradient for 20,000 PODS®-rhBDNF from Day 1–7. Note that  
<sup>370</sup> the BDNF concentrations were greater on D2–5 to promote neuronal differentia-  
<sup>371</sup> tion and neurite outgrowth observed on D7 (Figure 5B). Computed diffusion flux

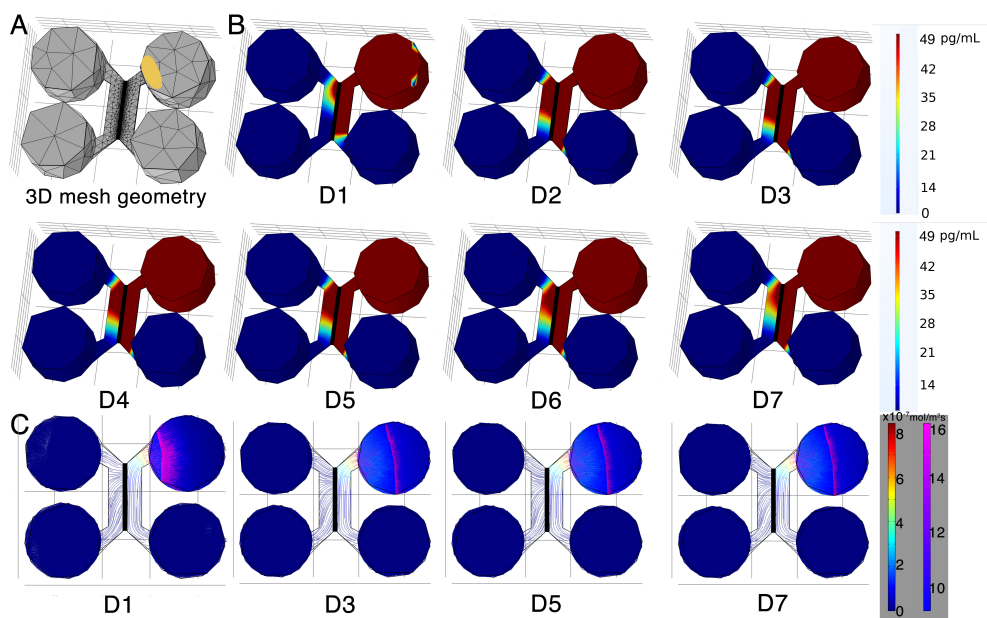


Figure 5: (A): 3D mesh geometry of a Xona™ XC450 created with Autodesk Inventor. An ellipse-shaped PODS®-rhBDNF disc is shown in yellow. (B): Human BDNF concentration gradient for 20,000 PODS®-rhBDNF from D1–D7. Note that the model does not account for media changes during the culture period. The corresponding color map is shown a range from 0 ng/mL to 49 ng/mL. (C): Diffusion flux ( $mol/m^2 s$ ) was computed using COMSOL Chemical Engineering module on D1, D3, D5, and D7.

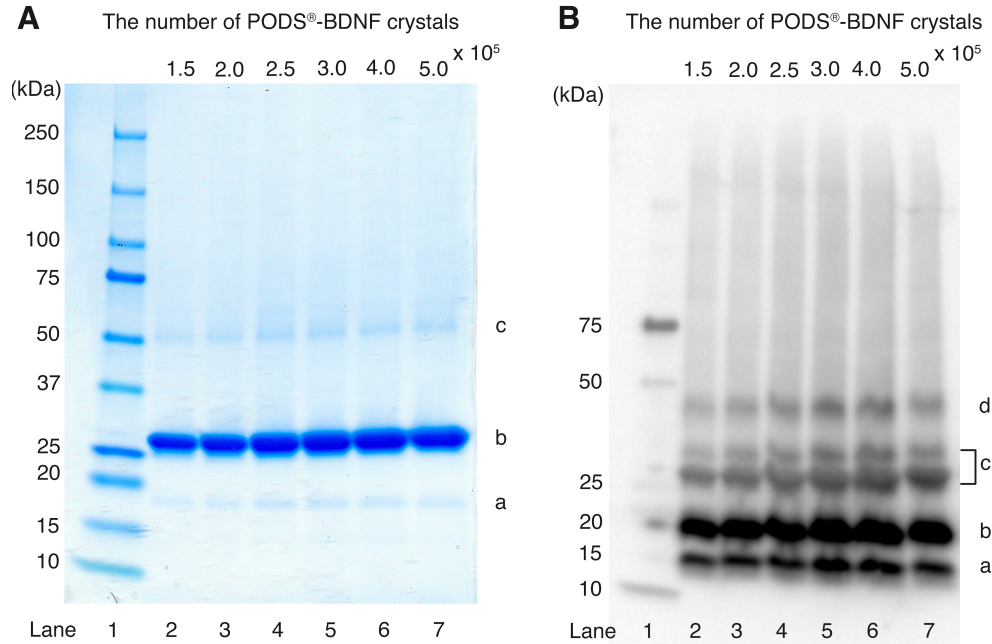


Figure 6: (A): SDS-PAGE analysis of PODS<sup>®</sup>-rhBDNF. Samples containing six quantities of PODS<sup>®</sup>-rhBDNF crystals were run on precast 4-15% polyacrylamide mini-gels and stained with Coomassie G-250 solution for visualization. Protein bands appear at approximately 18.8 (a), 28.0 (b), and 46.8 kDa (c). Lane 1: molecular weight marker. Lanes 2-7: samples containing

372 was uniform throughout D1–7 (Figure 5C). Also note that highest concentration  
 373 of rhBDNF released from PODS<sup>®</sup>-crystals was greater than 50 pg/mL, the  
 374 concentration sufficient for otic neuronal differentiation and neurite outgrowth  
 375 of hPSC-derived ONP 3D spheroids from our previously published data [9].  
 376 For the optimization process in determining the adequate number of PODS<sup>®</sup>-  
 377 rhBDNF, we also performed FEA with 10,000 and 40,000 PODS<sup>®</sup>-rhBDNF.  
 378 Please see detailed discussion of how we determined the optimum concentration  
 379 of 20,000 PODS<sup>®</sup>-rhBDNF in Supplementary Figure S8.

380 SDS-PAGE was used to separate PODS<sup>®</sup>-rhBDNF crystals into its con-  
 381 stituent proteins to determine the molar ratio of polyhedrin to BDNF. Visu-  
 382 alization with Coomassie G-250 solution (Figure 6A) revealed three distinct

383 protein bands at 18.8 (a), 28.0 (b), and 46.8 (c) kDa, which correspond with  
384 the molecular weights of H1-tagged BDNF monomer, polyhedrin, and H1-tagged  
385 BDNF monomer attached with polyhedrin, respectively. Western blot analy-  
386 sis was subsequently conducted to confirm the identity of the 18.8 kDa band  
387 as rhBDNF. Enhanced chemiluminescence (Figure 6B) revealed four protein  
388 bands at 14.0 (a), 18.8 (b), 37.6 (c), and 46.8 (d) kDa, which correspond with  
389 the molecular weights of rhBDNF monomer, H1-tagged BDNF monomer, H1-  
390 tagged BDNF dimer, and H1-tagged BDNF monomer attached with polyhedrin.  
391 Immunoblot detection of the 18.8 kDa band further implicates its identity as  
392 rhBDNF. SDS-PAGE images were converted to 8-bit grayscale and mean cor-  
393 rected integrated pixel intensity values were calculated for protein bands located  
394 at 28.0 and 18.8 kDa; the protein band detected at 46.8 kDa was omitted from  
395 the final computation based on the notion that it contained a 1:1 ratio of poly-  
396 hedrin to BDNF. Results indicate that the molecular ratio of polyhedrin to  
397 rhBDNF is approximately 17:1.

398 To objectively compare the degree of otic neuronal differentiation in hPSC-  
399 derived ONPs, we performed quantitative analysis of PAX8 and GATA3 double-  
400 positive cells using immunocytochemistry. We chose PAX8 and GATA3 for this  
401 analysis because our previous studies indicated high expression of these protein  
402 markers in late-stage ONPs and early-stage SGNs [8, 9, 24]. Cells were stained in  
403 the somal compartment of the Xona™ device, highlighted in green in Figure 7A.  
404 Figure 7B shows the resulting image of cells in the somal compartment, and  
405 a heat-map representation of the percentage of double-positive cells is shown  
406 in Figure 7C. It should be noted here that the heatmap is sensitive to the  
407 differences in cell density across channel. This was accounted by averaging  
408 the double-positivity across three biological replicates. The heat-map indicates  
409 higher double-positivity in the upper region of the somal compartment, which  
410 is closest to the PODS®-rhBDNF disc placement (shown in a orange ellipse in  
411 Figure 7A) in the neurotrophin compartment. Double-positivity decreases in  
412 the somal compartment as distance from the PODS®-rhBDNF disk increases,  
413 supporting the presence of a BDNF neurotrophin gradient as predicted by our

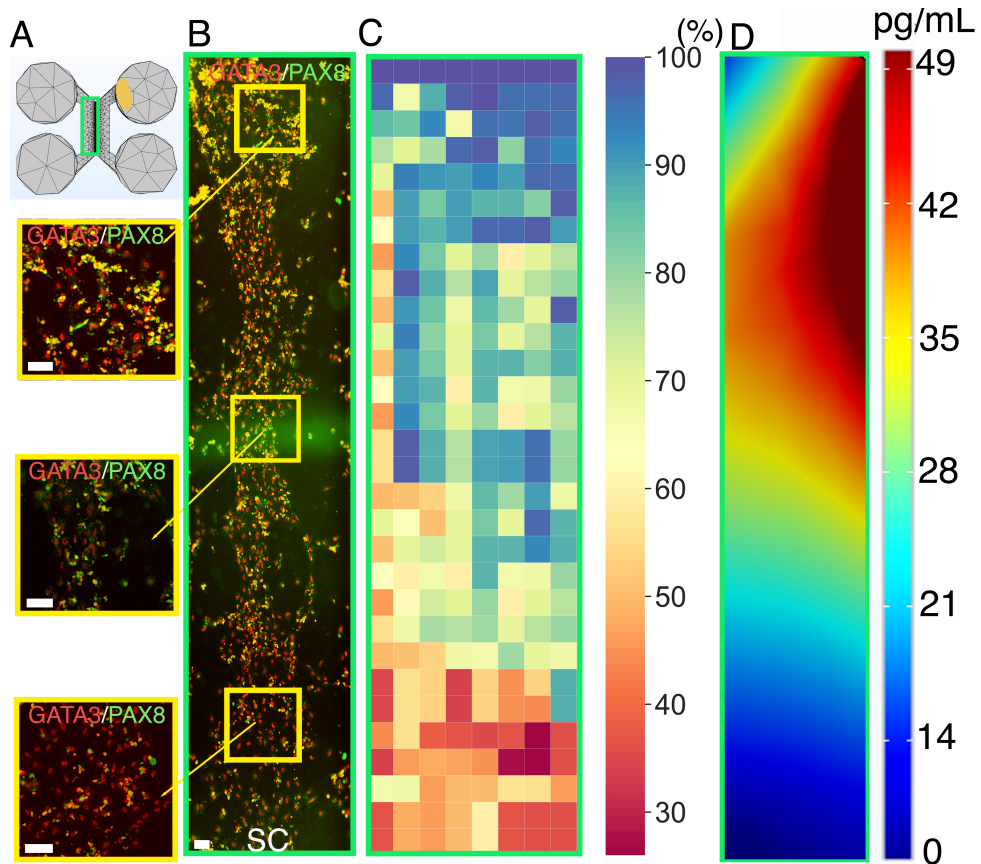


Figure 7: Human PSC-derived late-stage ONPs grown in a microfluidic device at Day 7 were stained for GATA3 (red) and PAX8 (green). (A): Geometry mesh of the microfluidic device Xona™ XC450 generated by Autodesk Inventor. The green square indicates the cell seeding location in the somal compartment of the device. An ellipse-shaped PODS®-rhBDNF disc is shown in yellow. (B): Cells were analyzed by staining with neuronal markers GATA3 (red) and PAX8 (green). Yellow highlighted regions are magnified on the left. SC: somal compartment. (C): Heat-map representation of double-positivity of hPSC-derived ONPs in the device for GATA3 and PAX8 ( $n = 3$ ). Double-positivity increases from the lower to the upper portion of the somal compartment, suggesting that the higher BDNF concentration in the upper portion of the device improves differentiation. Scale bar: 100  $\mu\text{m}$ . (D): Prediction of BDNF concentration gradient released from PODS®-rhBDNF at seven days in culture using a finite element model. The corresponding color map is shown with a range from 0–49 pg/mL.

414 computational model calculation (Figure 7D).

415 We defined two hypothetical directional angles to predict the orientation of  
416 hPSC-derived ONPs and neurite growth (Figure 8). The  $n$ -dimensional Eu-  
417 clidean space, denoted by  $\mathbb{R}^n$ , is a linear vector space in that we can use polar  
418 coordinates to compute the directionality of cells and neurites [45]. Here, we  
419 used  $n = 1$  and 2. For one-dimensional Euclidean space ( $n = 1$ ), we simply drew  
420 a line for the Euclidean distance—the shortest distance between two points as  
421 shown in Figure 8A(b) (dark green lines). The two points were 1) the center  
422 point of a PODS®-rhBDNF disk ( $P$ ) and 2) the mid point of the medial side  
423 ( $Q_{1-5}$ ) (i.e., the near side to microgroove channels) of a pre-designated square  
424 (shown as a black square, zone 1–5 in Figure 8), respectively. The Euclidean  
425 distance angle (EDA),  $\phi_i$ , was defined as the angle between the horizontal line  
426 zero direction and the line  $PQ_i$  that consists of the Euclidean distance where  $i$   
427 = 1–5.

428 For two-dimensional Euclidean space ( $n = 2$ ), we utilized Fick's first law,  
429 which dictates that the diffusion flux ( $D$ ) is proportional to the concentration  
430 gradient ( $C$ ) [46]. Based on this theorem, the direction of a flow vector can  
431 be used to represent concentration gradient for the directionality. We hypothe-  
432 sized here that cell orientation is directionally controlled by the flux vector  
433 which is driven by the concentration gradient. Figure 8B shows the flow vectors  
434 in a somal compartment at Day 7 computed by COMSOL Chemical engineering  
435 module. We averaged the 10 flow vectors in each of five zones in Figure 8 to  
436 compute diffusion flux angle (DFA),  $\psi_i$ , where  $i = 1–5$  in Figure 8. To lighten  
437 the computational intensity, we reduced a dimension from 3D to 2D to com-  
438 pute diffusion Flux. Please see justification in Supplementary Data. All of the  
439 computed EDAs and DFAs can be found in Supplementary Table 2.

440 Figure 9 shows time-series of microscopic phase-contrast photomicrographs  
441 obtained on Day 1, 3, and 7 in the five zones in a Xona™ XC450. Each preferred  
442 orientation of any given cell was computed and then plotted on a polar diagram  
443 (blue circle). Mean vector angle (MVA, shown in red line on Figure 9) and  
444 median vector angle were computed. All of the polar diagrams in Figure 9 show

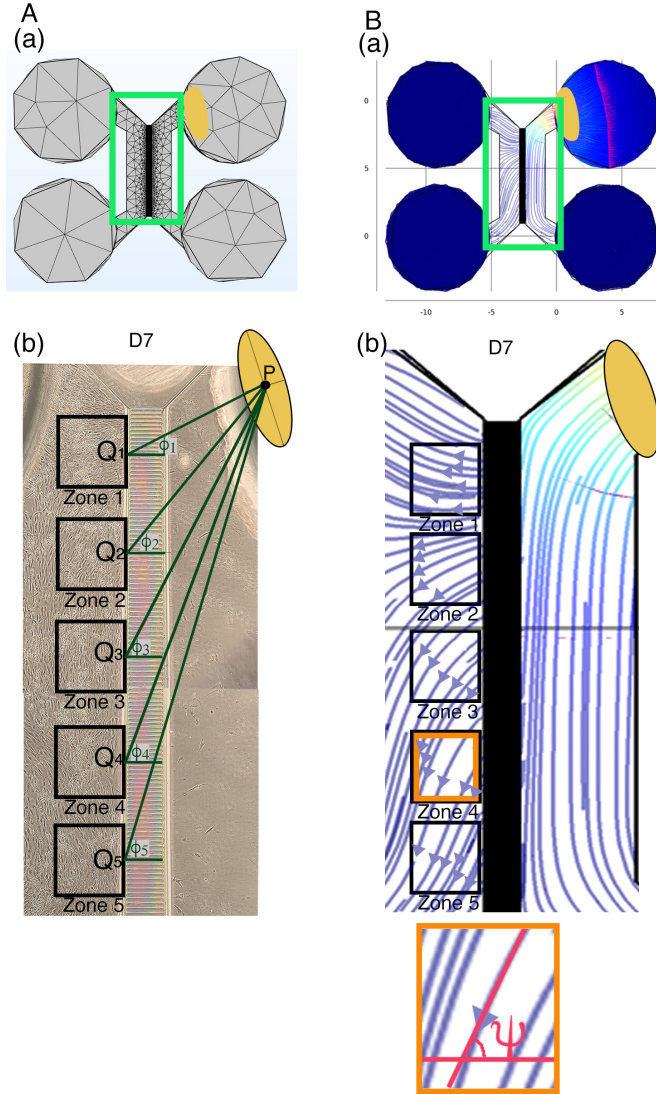


Figure 8: (A): Defining the Euclidean distance angle (EDA). (a) X-Y plane geometry mesh of a Xona™ XC450 device. Green square shows an area corresponding to a phase-contrast image below. An ellipse-shaped PODS®-rhBDNF disc is shown in yellow. (b) hPSC-derived ONPs were cultured in a Xona™ XC450 for seven days (D7). Yellow ellipse once again indicates the location of a disk contains PODS®-rhBDNF crystals (P: the center of this ellipse). In the somal compartment of the Xona™ XC450 device, we defined Zone 1–5, shown in black square. A line was drawn from the center of the PODS®-rhBDNF disk (P) to (Q<sub>1–5</sub>) (i.e., the near side to microgroove channels) of a pre-designated square (shown as a black square, zone 1–5) [i.e.,zone 1–5]. The Euclidean distance angle (EDA) for zone 1–5 was defined as  $\phi_i$ ,  $i = 1–5$ . (B): Defining diffusion flux angle (DFA). (a) Diffusion flux in a Xona™ XC450. Green squared area show a somal and neurotrophin compartment, which are magnified in (b). (b) Magnified image of diffusion flux of Zone 1–5 in a Xona™ XC450. Orange highlighted zone (zone 4) was magnified at the bottom of (b), defining a DFA ( $\psi$ ).

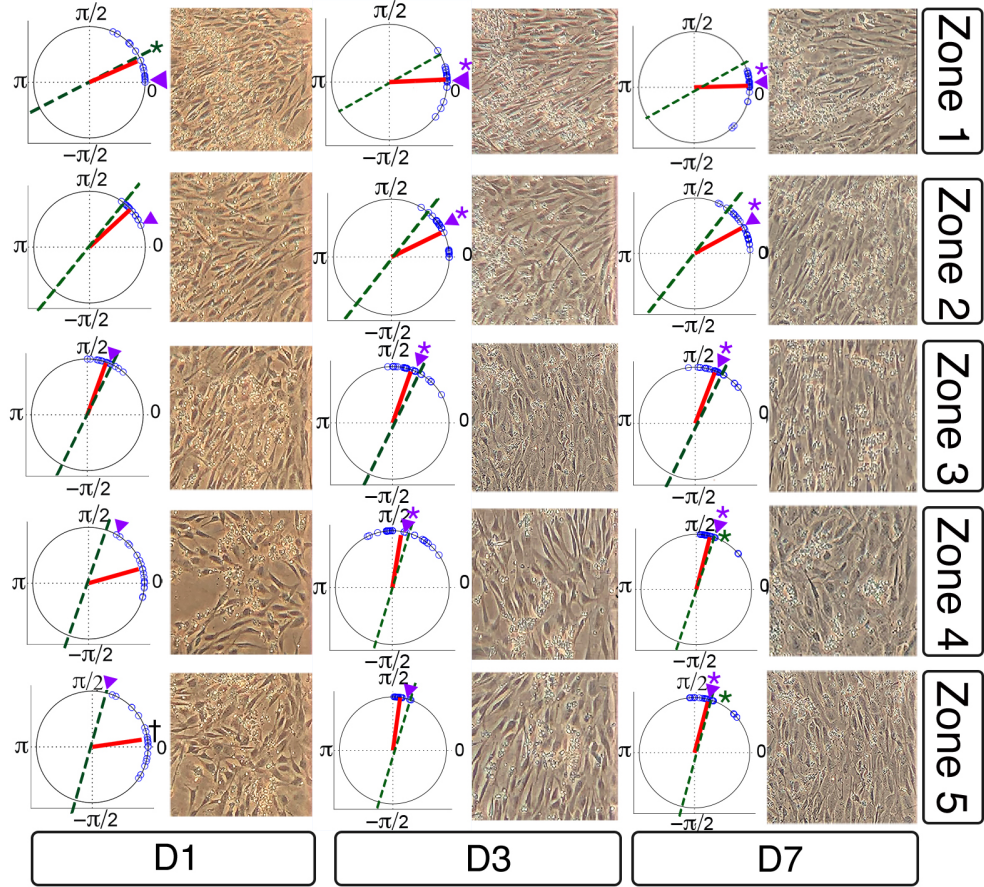


Figure 9: Preferred cell orientation analysis. Sequential phase-contrast images of a somal compartment of a Xona™ XC450 device in zone 1–5 (see Figure 8) on day 1 (D1), day 3 (D3), and day 7 (D7). A corresponding polar histogram indicates preferred orientation of hPSC-derived ONPs in an angle ( $0$ – $2\pi$  radians) in blue circles. Mean vector angle is shown in red line. Green dotted line shows Euclidean Distance Angle (EDA) and purple triangle indicates Diffusion Flow Angle (DFA). † symbol indicates that  $p$  value  $> 0.01$ . \* symbol indicates that the mean vector angle fits within the 95% confidence internal ( $\alpha < 0.05$ .)

445 that preferred orientation of hPSC-derived ONPs distribute in an unimodal dis-  
446 tribution. We also confirmed that a von Mises distribution is appropriate for  
447 these sets of data (See Supplementary Figure S9). We, therefore, then tested  
448 further to see if the cells had tendency to be oriented to a certain direction.  
449 To test this hypothesis, we used the Rayleigh test of uniformity to evaluate  
450 whether there is statistical evidence of circular directionality [32]. Computed  
451 *p* values for all the 15 conditions were less than 0.05, demonstrating that all  
452 of the conditions had statistically significant directionality. To further validate  
453 whether the observed angles have a tendency to cluster around the two hypo-  
454 thetical angles (i.e., EDA and DFA), we then performed the V test. Once again,  
455 *p* values for all 15 conditions were less than 0.05 except one (Zone 5 on Day 1),  
456 re-demonstrating that most of the conditions had statistically significant ten-  
457 dencies to cluster around the EDAs and DFAs. Finally, to investigate whether  
458 the preferred orientation of the cells were clustered around the EDAs or DFAs,  
459 we performed one sample test for the mean vector angle, which is similar to a  
460 one sample t-test on a linear scale. There was only one condition (Zone 1, day  
461 1) that was statistically significant for EDA, whereas most of the conditions on  
462 Day 3 and 7 were statistically significant for DFA. Therefore, our results here  
463 demonstrated that hPSC-derived ONPs had greater tendency to cluster around  
464 DFA than EDA. All computed statistical values are shown in Supplementary  
465 Table S2.

466 To evaluate the direction of neurites of hPSC-derived ONPs, we first de-  
467 fined EDA in Region 1-3 ( $\phi'_j$ ,  $j = 1 - 3$ ) (Figure 10A) and DFA ( $\psi'_j$ ,  $j = 1 - 3$ );  
468 similarly defined  $\phi_i$  and  $\psi_i$  as in Figure 8. All of the EDAs and DFAs defined  
469 here can be found in Supplementary Table S3. Polar histograms of the neurite  
470 direction angle in Region 1–3 indicated that the two longest neurites were bi-  
471 modal in nature (Figure 10B). In contrast, polar histograms of those cultured  
472 with rhBDNF (negative control) and 800,000 PODS®-BNDF (positive control)  
473 did not indicate bimodal distribution—the neurites did not show directionality  
474 (Figure 10C). The Rayleigh test of uniformity for both the positive and negative  
475 control were greater than 0.05, demonstrating that both of the conditions had

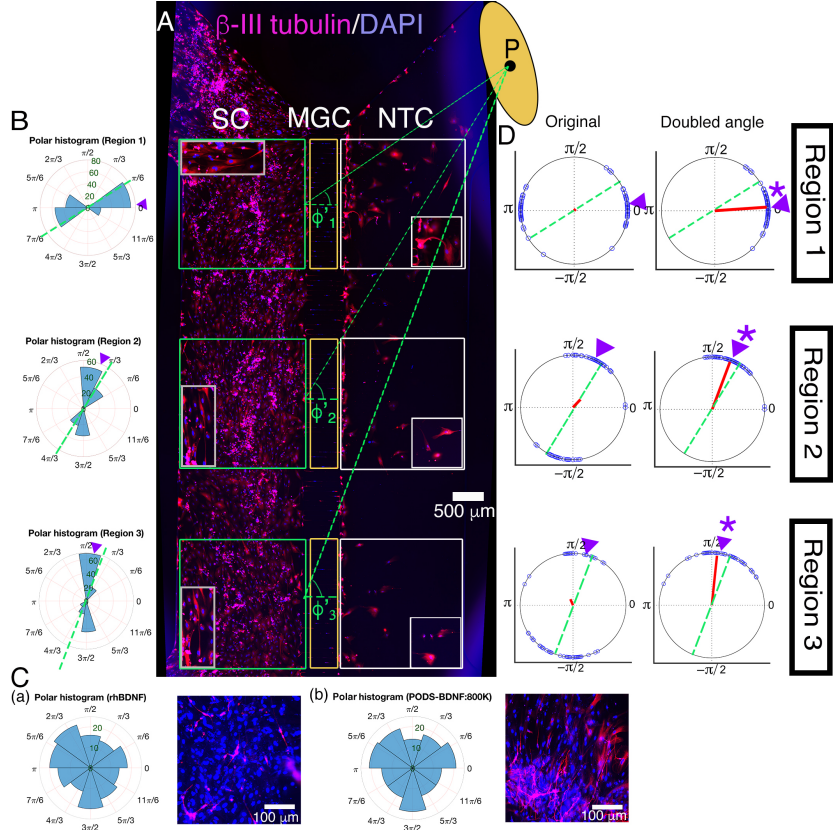


Figure 10: (A): Immunohistochemistry of hPSC-derived ONPs cultured in the Xona™ XC450 for seven days with  $\beta$ -III-Tubulin (pink fluorescence) and DAPI (blue fluorescence). A green line was drawn from the center of the BDNF disk (P) to the mid point of each of three pre-determined squares (Region 1–3) in the somal compartment to define Euclidean Distance Angle (EDA:  $\phi_i^c$ ,  $i = 1 - 3$ ). Green square: somal compartment (SC); yellow square: microgroove channels (MGC); White square: Neurotrophin compartment (NTC). High-power magnified images of the NTC and SC are shown. An ellipse-shaped PODS®-rhBDNF disc is shown in yellow. P: the center of the disk.(B): Polar histogram of neurite directional angles of hPSC-derived ONPs in the Xona™ XC450 at Day 7 (D7). The two longest neurites were measured. EDA: green dotted line. DFA: purple triangle. (C): (a) Right: Polar histogram of neurite directional angles of hPSC-derived ONPs cultured with 20 ng/mL of recombinant human BDNF for seven days. Left: Corresponding photomicrograph of immunocytochemistry with  $\beta$ -III tubulin (pink) and DAPI (blue). (b) Right: Polar histogram of neurite directional angles of hPSC-derived ONPs cultured with 800,000 of PODS®-rhBDNF for seven days. Left: Corresponding photomicrograph of immunocytochemistry with  $\beta$ -III tubulin (pink) and DAPI (blue). (D): A circular plot of neurite directional angle of hPSC-derived ONPs in Region 1–3. Once again, the two longest neurites were plotted on a unit circle. Right column: Original directional angle distribution. Left column: the method of doubling the angle applied to the original data. Each datum point is shown as a blue circle. Mean vector angle is shown as a red line. Green dotted line shows Euclidean Distance Angle (EDA) and purple triangle indicates Diffusion Flow Angle (DFA). \* symbol indicates that the mean vector angle fits within the 95% confidence internal ( $\alpha < 0.05$ .)

476 no statistically significant directionality (Supplementary Table S3: highlighted  
477 in green). We also analyzed the direction of the neurites using circular statistics.  
478 To obtain more realistic mean vector angles, we doubled each angle and reduced  
479 the multiples modulo 360°. In circular statistics, the bimodal distributed data  
480 can be transformed into a unimodal data by doubling the angle [32]. The mean  
481 vector angles in Figure 10D (right column) indicates the situation where the  
482 vectors were canceled out between the two groups of angles distributed in a bi-  
483 modal fashion, resulting in inaccurate representation. A circular plot in Figure  
484 10D (right column) showed doubled angles, representing actual representation  
485 of the neurite vector angles. In all of the three regions, the Reyleigh test and V  
486 test for EDA and DFA indicated directionality (Supplementary Table S3). One  
487 sample test for the mean vector angles in Region 1–3 indicated that they were  
488 not statistically different from DFA, but all of the three mean vector angles were  
489 statistically different from EDA.

490 We also stained the devices for  $\beta$ -III tubulin to track neurite growth and  
491 extension across the micro-groove channels as well as cell migration in three  
492 selected regions (Figure 10A). The location of the PODS®-rhBDNF disk in  
493 relation to the regions of interest in Figure 11A is indicated by a yellow circle.  
494 Quantitative analyses were performed and summarized in Figure 11B. Our data  
495 indicate that neurite length is dependent on BDNF concentration, with greater  
496 amounts of PODS®-rhBDNF promoting longer neurite growth (Figure 11B(a)).  
497 Lesser amounts of PODS®-rhBDNF, however, are necessary to create an ap-  
498 propriate concentration gradient. In the presence of 20,000 PODS®-rhBDNF,  
499 both neurite extension into the microchannels and cell migration into the neu-  
500 rotrophin compartment are greatest in the region closest to the BDNF source  
501 and decrease further from the PODS®-rhBDNF (Figure 11B(b,c)). Cell migra-  
502 tion is dependent on the distance from the source of BDNF, thus suggesting the  
503 presence of a BDNF gradient as predicted by our model. Note that the Xona  
504 microchannels intended to prevent from migration across channels.

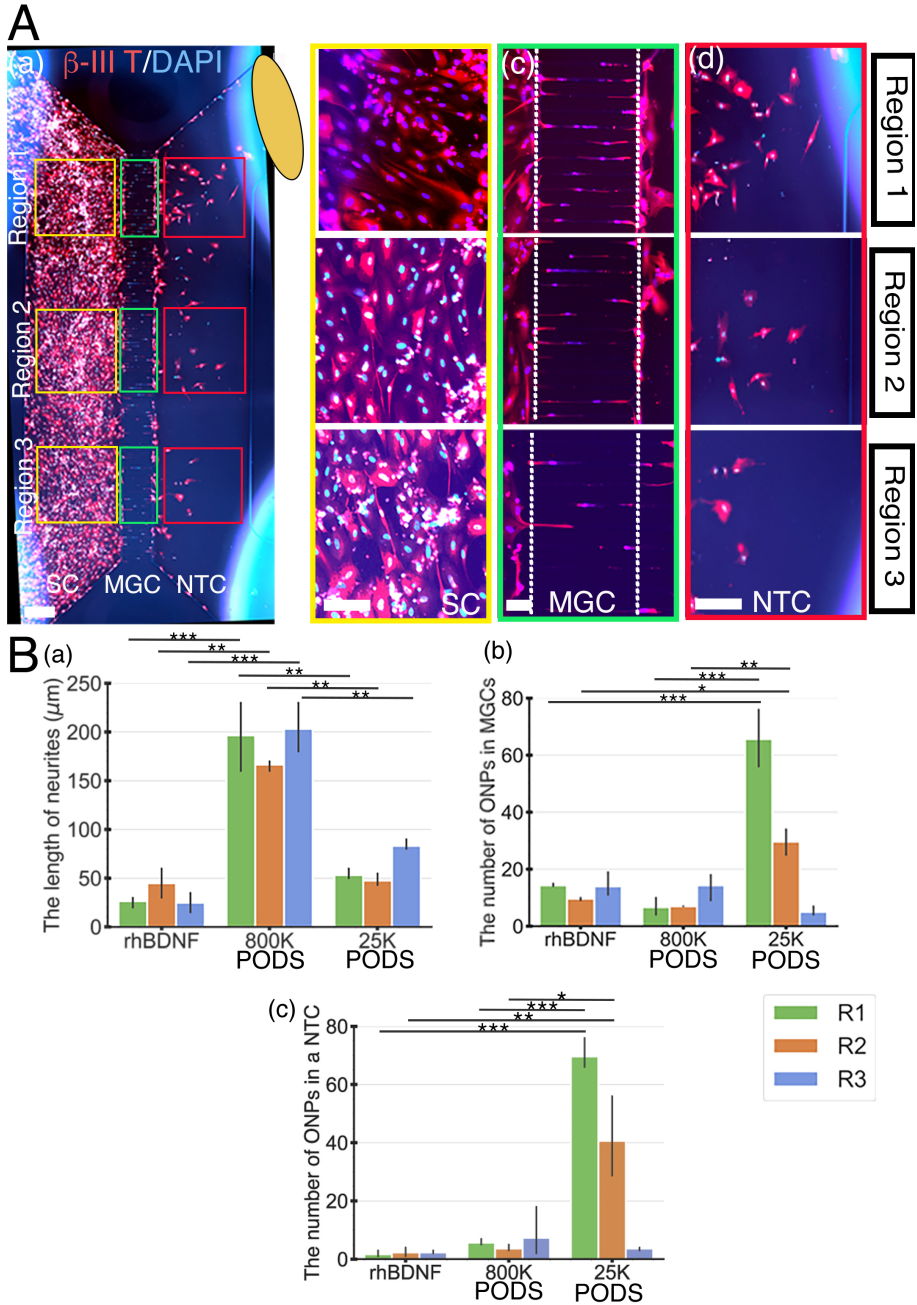


Figure 11: Human PSC-derived late-stage ONPs in the microfluidic device were stained with  $\beta$ -III tubulin (red) and DAPI (blue) to measure cell migration. (A): Late-stage ONPs stained after seven days in culture (a) with regions highlighted and magnified in the somal compartment (b), microgroove channels (c), and neurotrophin compartment (d). SC: somal compartment, MGC: microgroove channels, NTC: neurotrophic compartment. An ellipse-shaped PODS®-rhBDNF disc is shown in yellow. Scale bar (a): 500  $\mu\text{m}$ ; (b)–(d): 100  $\mu\text{m}$ . (B): Quantitative analyses of cell migration and neurite extension in devices using recombinant human BDNF, 800,000 PODS®-rhBDNF, or 20,000 PODS®-rhBDNF. \* :  $p < 0.05$ , \*\*:  $p < 0.01$ , \*\*\*:  $p < 0.001$ .

505    **4. Discussion**

506    *4.1. Challenges in neurotrophin treatment in the inner ear*

507    This is a proof-of-concept study for the realization of a neurotrophic strip  
508    to ascertain its scientific/technological parameters in a controlled *in vitro* en-  
509    vironment. Neurotrophin gradients have been studied for in multiple contexts  
510    [47, 48, 49]. However, it has not been feasible to reliably provide such a gra-  
511    dient to neurons neither *in vitro* nor *in vivo*, primarily because of technical  
512    challenges. While neurotrophin treatment has been recognized as a potential  
513    treatment for sensorineural hearing loss, there has not been clinical success in  
514    this avenue to date. Most recent relevant clinical trials used adeno-associated  
515    virus (AAV2) to deliver BDNF to the brain [50]. Although exciting, this treat-  
516    ment does not attempt to control the concentration of BDNF, which could  
517    potentially interfere with normal functions in a target organ [51]. Furthermore,  
518    this treatment may not be applicable to the inner ear. In this study, we used  
519    PODS®-rhBDNF to provide a neurotrophic gradient in a controlled fashion.  
520    Our result indicated 20,000 PODS-BDNF allowed for rhBDNF neurotrophin  
521    gradient such that hESC-derived ONPs survived, differentiated toward human  
522    SGNs, and also established directional neurite outgrowth in a microfluidic device.

523    *4.2. Microfluidic device-generated gradient*

524    We used a microfluidic device to advance our understanding of directional  
525    neurite growth and otic neuronal differentiation in response to a BDNF concen-  
526    tration gradient [52]. Among many *in vitro* concentration gradient sustaining  
527    culture devices, microfluidic devices have overcome many of the deficits that  
528    conventional platforms (i.e., the Boyden chamber, Dunn chambers, or compart-  
529    mentalized diffusion chambers) face [52]. Conventional platforms tend to be sub-  
530    optimal to manipulate small volumes of fluid at the order of microliters. Growth  
531    factors and proteins are used in minute amounts in our microfluidic device, and  
532    cultured stem cells are able to interact with endogenous factors. As mentioned  
533    earlier, this micro-environment more accurately represents *in vivo* conditions.

534 The Xona™ device can be used to sustain a three-dimensional concentration gra-  
535 dient over time (duration dependent on the half-life of the molecule) due to its  
536 microchannel array. The device limits convective flow in the gradient-forming  
537 areas by introducing microgroove channels that generate high fluidic resistance,  
538 thereby limiting flow to diffusion. The high resistance of the microchannel array  
539 also prolongs diffusion across them, thereby increasing both gradient formation  
540 and gradient steepness. These features allowed us to generate a FEM, which pre-  
541 dicted the necessary number of PODS®-BDNF crystals for a BDNF gradient.  
542 Note, however, that this environment is different from the micro environment  
543 in the inner ear. A mesh geometry of the cochlea will be needed to compute the  
544 PODS®-BDNF crystal number for our next step of this study.

545 *4.3. BDNF and Polyhedrin protein*

546 Over the course of past 20–30 years, it has been established that BDNF me-  
547 diates survival and differentiation activities on SGNs by binding and activating  
548 the tyrosine kinase receptor kinase B (TrkB), a member of the larger family  
549 of Trk receptors [20]. Numerous studies have reported that BDNF can palliate  
550 SGN degeneration in ototoxically deafened animals, a widely accepted model for  
551 retrograde trans-synaptic SGN degeneration secondary to hair cell destruction  
552 [13, 14, 53, 54]. Additionally, it has been confirmed that there is a positive corre-  
553 lation between SGN counts and CI performance [55]. It is then safe to presume  
554 that treating CI recipients with BDNF would enhance overall CI performance,  
555 by preserving SGNs and their neurites. However, simply introducing rhBDNF  
556 into the inner ear poses significant hurdles. Although promising, human BDNF  
557 treatment has not been currently implemented in the inner ear. Unsuccessful  
558 BDNF treatment can be explained by several factors [56].

559 The blood half-life of BDNF protein is extremely short, only 1–10 min in  
560 the plasma [57, 58] and one hour in CSF [59]. The BDNF's high degrada-  
561 tion rate would require continuous replenishment, impractical for clinical use.  
562 Furthermore, introduction of a homogeneous solution of BDNF would promote  
563 nondirectional neurite growth where directed neurite growth is essential for de-

signing our new-generation bioactive CI, as depicted in Figure 1A. Directing neurite growth towards the CI electrode array is pivotal in the ultimate goal of enhancing performance through the narrowing of the electrode-neuron gap. The PODS® system precludes the phenomena by its localized, gradual release of growth factor. The steady supply of BDNF from a localized origin not only creates a concentration gradient, but maintains it over time. As seen in Figures 4–6, we were able to perform a finite element analysis based on data we collected describing the chemical release kinetics and molar ratio of PODS®-BDNF system. It is clearly visible that the slow-release nature of PODS®-BDNF results in a concentration gradient over the course of Day 1–7 (Figure 5).

It should be noted that our FEM assumes free diffusion of the rhBDNF protein. In biological cell-culture conditions, BDNF released from PODS®-BDNF has tendency to adhere to the walls of the culture device because BDNF is a “sticky” protein of about 27 kDa (mature BDNF dimer) and it is positively charged under physiological conditions (isoelectric point, pI = 9.4) [60]. As such, the physio-chemical properties of BDNF have made the recombinant protein difficult to diffuse. This phenomenon was observable in preliminary data where the ONPs failed to survive past 1–3 days of culture (data not shown). To circumvent this issue we infused the culture media with a carrier protein (i.e., BSA), hypothesizing that the albumin would act as a carrier for the released BDNF and allow for free diffusion throughout the microfluidic device [61]. This hypothesis is supported by our sets of biological verification data (Figures 7–11) that clearly shows that hPSC-derived ONPs responded to the modification by exhibiting the expected cell body orientation, unidirectional neurite extension, and neurite length. Note that albumin is the single protein found in highest concentrations in the perilymph [62], therefore, a carrier protein will not be needed in our future *in vivo* study.

#### 4.4. Intracellular signaling initiated by Thyrosine kinase B receptor

Another issue we need to consider in interpretation of our results is the intracellular cell signaling mechanism elicited by rhBDNF. Human BDNF (mature

594 dimeric form) binds with high affinity to its TrkB receptor. The binding of  
595 BDNF to a TrkB receptor has proven to have significant importance for the  
596 proneuronal effects of BDNF [20]. Upon binding BDNF, TrkB dimerizes, and  
597 activates intrinsic kinase activities and other complex set of intracellular sig-  
598 naling cascades, which is beyond the scope of this study. However, it should  
599 be noted that activation of TrkB receptor by neurotrophin binding causes the  
600 TrkB protein to be internalized in endosomes on the cellular membrane [63].  
601 Endosomes can then be transported to the soma. Therefore, the proneuronal  
602 effects of rhBDNF in our results might have highly depended on the status of  
603 TrkB receptors on the cell membrane of hPSC-derived ONPs. Our previous  
604 study has demonstrated that strong expression of a TrkB receptor on derived  
605 ONPs [24], however, more detailed studies on TrkB receptors on hPSC-derived  
606 ONP and SGNs will be needed.

607 *4.5. Degradation of PODS® crystals by protease*

608 In cell culture, degradation of PODS®-rhBDNF is likely due to the activity  
609 of cell-secreted proteases. The proteases break down the peptide bonds of the  
610 encasing polyhedrin protein, creating openings in the structure to allow release  
611 of the rhBDNF. Therefore, the presence of proteases is imperative for the proper  
612 utilization of the PODS® crystals. Additionally, these proteases are responsible  
613 for the degradation of the released BDNF. Because stem cells are not present  
614 in the culture media used for the PODS® degradation kinetics experiments, we  
615 infused the media with 10% FBS, which naturally contains proteases, to promote  
616 polyhedrin degradation, BDNF release, and BDNF degradation to attain results  
617 that more accurately describe *in vitro* events. Moreover, since the cells and  
618 PODS are initially segregated into separate compartments within the culture  
619 device, cell-secreted proteases are unlikely to reach and degrade the PODS in  
620 time to support ONP survival and differentiation. Infusion of FBS was therefore  
621 required in these experiments as well. In clinical use, however, we presume  
622 that cell-secreted proteases will be readily present in the inner ear and would  
623 therefore preclude the need for artificial supplementation.

624     *4.6. A concept design: Neurotrophic strip*

625     The plateau in CI performance in treatment of sensorineural hearing loss has  
626     driven researchers to develop innovative supplementary treatment strategies to  
627     push the field past this hurdle. Our approach strives to directly address the  
628     issue at its core: the electrode-neuron gap, which can lead to serious implica-  
629     tions include low spatial frequency resolution and high power consumption. We  
630     can use our data as a launchpad for the neurotrophic strip (NS). The NS is a  
631     biointerface concept that integrates an extended-release source of growth factor  
632     to facilitate a protein gradient. Implanted in conjunction with the CI, it acts  
633     as a bridge between the extant SGNs and implanted late-ONPs grown on the  
634     electrode itself. The NS would promote survival of both cell populations, dif-  
635     ferentiation of the late ONP implants, promote directional neurite growth and  
636     synaptogenesis between the two, effectively creating a neuronal network between  
637     the patient and the implanted CI. Each electrode would be able to stimulate cell  
638     bodies at exceptionally high resolution, essential for greater intonation differ-  
639     entiability (required for effective social interaction and music appreciation) and  
640     so, increased quality of life for millions. Our successful outcomes are essential  
641     to make a neurotrophic strip feasible in *in vivo* environment.

642     *4.7. The limitations of this study and future direction*

643     There are some limitations associated with this study. First, the reduction of  
644     spacial dimension to 2D for diffusion modeling certainly affected the flux vector,  
645     which determines the predicted concentration vector. Given that the thickness  
646     (i.e., Z-axis) of the microfluidic device was 100  $\mu\text{m}$ , we estimated that the effect  
647     was minimal. In the future, we plan to use PSC-derived 3D spheroids in a somal  
648     compartment so that flux vector and concentration gradient vector can more  
649     accurately model the cell behavior. In this way, we will be able to circumvent  
650     the need to reduce diffusion calculations to 2D for computation performance in  
651     the modeling.

652     Secondly, we required to generate a model in that the BDNF's biological  
653     transportation phenomenon from a PODS<sup>®</sup>-rhBDNF disk to a somal compart-

654 ment of a Xona™ device. Note that in this model, we focused on the major  
655 dependent variable, BDNF concentration gradient to model the biological phe-  
656 nomenon. Other physical variables to promote cell migration, otic neuronal  
657 differentiation, and neurite growth were not take into consideration. These  
658 variables include electotaxis (electrical potential), durotaxis (matrix's stiffness  
659 [i.e., laminin 511 in our case]) [64], mechanotaxis (cell strain), and lastly cell  
660 migration by random walk [65]. In our future study, we will take these vari-  
661 ables into consideration to more accurately represent the migration and neurite  
662 growth of hPSC-derived ONPs.

663 Insufficient contrast between cells and background in phase contrast images  
664 led to inaccuracies in cell orientation computation for some images. To address  
665 this issue, poor quality images were disregarded in the quantitative analysis.  
666 We occasionally used manual measurement for accuracy. Our future study may  
667 entail automated time-series cell analysis, which would allow more accurate  
668 measurement. Also, another way to address this issue would be with a cell  
669 membrane staining in the future.

670 While 20,000 of PODS®-rhBDNF were necessary for hPSC-derived ONPs  
671 for otic neuronal differentiation and directional neurite outgrowth, this condi-  
672 tion may not be sufficient. For instance, it is still not known whether the effects  
673 of other neurotrophic factors such as Neurotrophin-3 and Glial cell line-derived  
674 neurotrophic factor could have a positive effect on ONP growth [20, 66, 67]. We  
675 are planning to investigate these neurotrophic factors in the future. Other fac-  
676 tors that could have an impact on directional neurite growth include endogenous  
677 factors secreted from hPSC-derived ONPs. While our previous study demon-  
678 strated that hPSC-derived ONPs only secreted negligible amount of BDNF that  
679 were detected by ELISA [9], currently we do not have any data on other neu-  
680 rotrophic factors or other molecules that could have affected directional neurite  
681 growth in the inner ear. We chose BDNF first to study because the most inten-  
682 sively studied neurotrophic factor in the field of hearing research is BDNF [20].  
683 Previous studies have indicated that neurotrophic supports of SGNs are mainly  
684 from BDNF and neurotrophin-3 (NT-3) [20, 60]. Therefore, the potential con-

685 founding effect of the secretions of other neurotrophic factors and molecules  
686 secreted from derived SGNs are likely NT-3, for which further investigation is  
687 necessary in the future.

688 Despite the aforementioned limitations associated in this study, the present  
689 results generated BDNF concentration gradient, condition of which is necessary  
690 for hPSC-derived ONPs to differentiate into the otic lineage (i.e., SGNs) and  
691 also promoted directional neurite extension towards the POD-BDNF disk. The  
692 technique will allow us to control neurite direction of transplanted hPSC-derived  
693 ONPs in the inner ear. We will harness this method in our design of a bioactive  
694 CI.

## 695 **Conclusions**

696 We were able to generate BDNF concentration gradient, enabling survival,  
697 neuronal differentiation toward SGNs, and directed neurite extension of hPSC-  
698 derived ONPs. The technique will allow us to control neurite direction of trans-  
699 planted hPSC-derived ONPs in the inner ear. This proof-of-concept study pro-  
700 vides a step toward next-generation bioactive CI technology.

## 701 **Acknowledgment**

702 This work was supported by the American Otological Society Clinician Sci-  
703 entist Award (AJM), the Triological Society/American College of Surgeons  
704 Clinician Scientist Award (AJM), the Department of Otolaryngology of North-  
705 western University (AJM), the NIH (NIDCD) K08 Clinician Scientist Award  
706 K08DC13829-02 (AJM), and the Office of the Assistant Secretary of Defense of  
707 Health Affairs through the Hearing Restoration Research Program (Award #:  
708 RH170013:WU81XWUH-18-0712). Imaging work was performed at the North-  
709 western University Center for Advanced Microscopy, which is generously sup-  
710 ported by NCI CCSG P30 CA060553 awarded to the Robert H. Lurie Com-  
711 prehensive Cancer Center, for which we thank Peter Dluhy, Constadina Ar-  
712 vanitis, Ph.D., David Kirchenbuechler, Ph.D., and Wensheng (Wilson) Liu,

713 M.D. Some of microfluidic device experiments were performed in the Analytical  
714 bioNanoTechnology (ANTEC) Core Facility of the Simpson Querrey Institute  
715 at Northwestern University, which is supported by the Soft and Hybrid Nan-  
716 otechnology Experimental (SHyNE) Resource (NSFECCS-1542205). We thank  
717 Shreyas Bharadwaj (Cornell University), Kyle Coots (Midwestern University),  
718 Andrew Oleksijew (the University of Nebraska), Duncan Chadly (California In-  
719 stitute of Technology), and Shun Kobayashi (the University of Texas at Austin)  
720 for their contribution to the earlier phases of this project. We thank Sara Dun-  
721 lop (Department of Neurology, Northwestern University), and Dr. Jacqueline  
722 Bond (the University of California San Diego) for assistance in Western Blot and  
723 SDS-Page gels. We also thank Dr. Georgia Minakaki (Department of Neurol-  
724 ogy, Northwestern University) on assistance in ELISA. Finally, our thanks and  
725 appreciation go to our collaborator, Dr. Christian Pernstich (Cell Guidance  
726 Systems), for continuous support and stimulating discussions on this project  
727 since 2015.

728 **References**

- 729 [1] J. G. Naples, M. J. Ruckenstein, Cochlear Implant., Otolaryngologic Clinics  
730 of North America 53 (1) (2020) 87–102. doi:10.1016/j.otc.2019.09.  
731 004.
- 732 [2] B. S. Wilson, M. F. Dorman, Cochlear implants: A remarkable past  
733 and a brilliant future, Hearing Research 242 (1-2) (2008) 3–21. arXiv:  
734 NIHMS150003, doi:10.1016/j.heares.2008.06.005.
- 735 [3] C. Frick, M. Müller, U. Wank, A. Tropitzsch, B. Kramer, P. Senn, H. Rask-  
736 Anderson, K. H. Wiesmüller, H. Löwenheim, Biofunctionalized peptide-  
737 based hydrogels provide permissive scaffolds to attract neurite outgrowth  
738 from spiral ganglion neurons, Colloids and Surfaces B: Biointerfaces 149  
739 (2017) 105–114. doi:10.1016/j.colsurfb.2016.10.003.

- 740 [4] S. Hahnewald, A. Tscherter, E. Marconi, J. Streit, H. R. Widmer, C. Gar-  
741 nham, H. Benav, M. Mueller, H. Löwenheim, M. Roccio, P. Senn, Response  
742 profiles of murine spiral ganglion neurons on multi-electrode arrays., Journal  
743 of neural engineering 13 (1) (2016) 16011. doi:10.1088/1741-2560/  
744 13/1/016011.
- 745 [5] R. K. Shepherd, S. Hatsushika, G. M. Clark, Electrical stimulation of  
746 the auditory nerve: The effect of electrode position on neural excitation,  
747 Hearing Research 66 (1) (1993) 108–120. doi:10.1016/0378-5955(93)  
748 90265-3.
- 749 [6] M. Tykocinski, L. T. Cohen, B. C. Pyman, T. Roland, C. Treaba, J. Palamara,  
750 M. C. Dahm, R. K. Shepherd, J. Xu, R. S. Cowan, N. L. Cohen,  
751 G. M. Clark, Comparison of electrode position in the human cochlea using  
752 various perimodiolar electrode arrays., The American journal of otology  
753 21 (2) (2000) 205–211. doi:10.1016/S0196-0709(00)80010-1.
- 754 [7] A. Roemer, U. Köhl, O. Majdani, S. Klöß, C. Falk, S. Haumann, T. Lenarz,  
755 A. Kral, A. Warnecke, Biohybrid cochlear implants in human neurosensory  
756 restoration., Stem cell research and therapy 7 (1) (2016) 148. doi:10.  
757 1186/s13287-016-0408-y.
- 758 [8] R. A. Heuer, K. T. Nella, H. T. Chang, K. S. Coots, A. M. Oleksijew,  
759 C. B. Roque, L. H. Silva, T. L. McGuire, K. Homma, A. J. Matsuoka,  
760 Three-dimensional otic neuronal progenitor spheroids derived from human  
761 embryonic stem cells, Tissue Engineering - Part A 27 (3-4) (2021) 256–269.  
762 doi:10.1089/ten.tea.2020.0078.
- 763 [9] H.-T. Chang, R. A. Heuer, A. M. Oleksijew, K. S. Coots, C. B. Roque, K. T.  
764 Nella, T. L. McGuire, A. J. Matsuoka, An Engineered Three-Dimensional  
765 Stem Cell Niche in the Inner Ear by Applying a Nanofibrillar Cellulose  
766 Hydrogel with a Sustained-Release Neurotrophic Factor Delivery System,  
767 Acta Biomaterialia 108 (2020) 111–127. doi:<https://doi.org/10.1016/j.actbio.2020.03.007>.

- 769 [10] L. Taylor, L. Jones, M. H. Tuszynski, A. Blesch, Neurotrophin-3 gradients  
770 established by lentiviral gene delivery promote short-distance axonal bridg-  
771 ing beyond cellular grafts in the injured spinal cord, *Journal of Neuroscience*  
772 26 (38) (2006) 9713–9721. doi:10.1523/JNEUROSCI.0734-06.2006.
- 773 [11] P. Senn, M. Roccio, S. Hahnwald, C. Frick, M. Kwiatkowska, M. Ishikawa,  
774 P. Bako, H. Li, F. Edin, W. Liu, H. Rask-Andersen, I. Pyykkö, J. Zou,  
775 M. Mannerström, H. Keppner, A. Homsy, E. Laux, M. Llera, J. P. Lel-  
776 louche, S. Ostrovsky, E. Banin, A. Gedanken, N. Perkas, U. Wank, K. H.  
777 Wiesmüller, P. Mistrík, H. Benav, C. Garnham, C. Jolly, F. Gander, P. Ul-  
778 rich, M. Müller, H. Löwenheim, NANOCI-Nanotechnology Based Cochlear  
779 Implant with Gapless Interface to Auditory Neurons, *Otology and Neuro-*  
780 *urology* 38 (8) (2017) e224—e231. doi:10.1097/MAO.0000000000001439.
- 781 [12] G. J. Goodhill, H. Baier, Axon Guidance: Stretching Gradients to  
782 the Limit, *Neural Computation* 10 (3) (1998) 521–527. doi:10.1162/  
783 089976698300017638.
- 784 [13] L. N. Gillespie, G. M. Clark, P. F. Bartlett, P. L. Marzella, BDNF-induced  
785 survival of auditory neurons *in vivo*: Cessation of treatment leads to ac-  
786 celerated loss of survival effects, *Journal of Neuroscience Research* 71 (6)  
787 (2003) 785–790. doi:10.1002/jnr.10542.
- 788 [14] L. N. Pettingill, R. L. Minter, R. K. Shepherd, Schwann cells geneti-  
789 cally modified to express neurotrophins promote spiral ganglion neuron  
790 survival *in vitro*, *Neuroscience* 152 (3) (2008) 821–828. doi:10.1016/j.  
791 *neuroscience*.2007.11.057. *Schwann*.
- 792 [15] R. K. Shepherd, A. Coco, S. B. Epp, Neurotrophins and electrical stim-  
793 ulation for protection and repair of spiral ganglion neurons following  
794 sensorineural hearing loss, *Hearing Research* 242 (2009) 100–109. doi:  
795 10.1016/j.heares.2007.12.005. *Neurotrophins*.
- 796 [16] B. Baseri, J. J. Choi, T. Deffieux, G. Samiotaki, Y. S. Tung, O. Olu-  
797 molade, S. A. Small, B. Morrison, E. E. Konofagou, Activation of sig-

- 798 naling pathways following localized delivery of systemically administered  
799 neurotrophic factors across the bloodbrain barrier using focused ultra-  
800 sound and microbubbles, Physics in Medicine and Biology 57 (7). doi:  
801 10.1088/0031-9155/57/7/N65.
- 802 [17] K. Ikeda, S. Nagaoka, S. Winkler, K. Kotani, H. Yagi, K. Nakanishi,  
803 S. Miyajima, J. Kobayashi, H. Mori, Molecular Characterization of Bom-  
804 byx mori Cytoplasmic Polyhedrosis Virus Genome Segment 4, Journal of  
805 Virology 75 (2) (2001) 988–995. doi:10.1128/jvi.75.2.988-995.2001.
- 806 [18] T. Suzuki, T. Kanaya, H. Okazaki, K. Ogawa, A. Usami, H. Watanabe,  
807 K. Kadono-Okuda, M. Yamakawa, H. Sato, H. Mori, S. Takahashi, K. Oda,  
808 Efficient protein production using a Bombyx mori nuclear polyhedrosis  
809 virus lacking the cysteine proteinase gene, Journal of General Virology  
810 78 (12) (1997) 3073–3080. doi:10.1099/0022-1317-78-12-3073.
- 811 [19] H. Mori, R. Ito, H. Nakazawa, M. Sumida, F. Matsubara, Y. Minobe,  
812 Expression of Bombyx mori cytoplasmic polyhedrosis virus polyhedrin in  
813 insect cells by using a baculovirus expression vector, and its assembly into  
814 polyhedra, Journal of General Virology 74 (1) (1993) 99–102. doi:10.  
815 1099/0022-1317-74-1-99.
- 816 [20] S. H. Green, E. Bailey, Q. Wang, R. L. Davis, The Trk A, B, C's of  
817 Neurotrophins in the Cochlea., Anatomical record (Hoboken, N.J. : 2007)  
818 295 (11) (2012) 1877–1895. doi:10.1002/ar.22587.
- 819 [21] I. Meyvantsson, D. J. Beebe, Cell culture models in microfluidic systems,  
820 Annual Review of Analytical Chemistry 1 (1) (2008) 423–449. doi:10.  
821 1146/annurev.anchem.1.031207.113042.
- 822 [22] Z.-J. Guo, M.-H. Yu, X.-Y. Dong, W.-L. Wang, T. Tian, X.-Y. Yu, X.-D.  
823 Tang, Protein composition analysis of polyhedra matrix of Bombyx mori  
824 nucleopolyhedrovirus (BmNPV) showed powerful capacity of polyhedra to  
825 encapsulate foreign proteins., Scientific reports 7 (1) (2017) 8768. doi:  
826 10.1038/s41598-017-08987-8.

- 827 [23] A. J. Matsuoka, Z. A. Sayed, N. Stephanopoulos, E. J. Berns, A. R. Wad-  
828 hwani, Z. D. Morrissey, D. M. Chadly, S. Kobayashi, A. N. Edelbrock,  
829 T. Mashimo, C. A. Miller, T. L. McGuire, S. I. Stupp, J. A. Kessler,  
830 Creating a stem cell niche in the inner ear using self-assembling peptide  
831 amphiphiles., *Plos One* 12 (12) (2017) e0190150. doi:10.1371/journal.  
832 pone.0190150.
- 833 [24] A. J. Matsuoka, Z. D. Morrissey, C. Zhang, K. Homma, A. Belmadani,  
834 C. A. Miller, D. M. Chadly, S. Kobayashi, A. N. Edelbrock, M. Tanaka-  
835 Matakatsu, D. S. Whitlon, L. Lyass, T. L. McGuire, S. I. Stupp, J. A.  
836 Kessler, Directed Differentiation of Human Embryonic Stem Cells Toward  
837 Placode-Derived Spiral Ganglion-Like Sensory Neurons, *Stem Cells Trans-  
838 lational Medicine* 6 (2017) 923–936. doi:10.1002/sctm.16-0032.
- 839 [25] H. Al-Ali, S. R. Beckerman, J. L. Bixby, V. P. Lemmon, In vitro models  
840 of axon regeneration, *Experimental Neurology* 287 (Pt 3) (2017) 423–434.  
841 doi:10.1016/j.expneurol.2016.01.020.
- 842 [26] U. K. Laemmli, Cleavage of structural proteins during the assembly of  
843 the head of bacteriophage T4., *Nature* 227 (5259) (1970) 680–685. doi:  
844 10.1038/227680a0.
- 845 [27] A. L. Mandel, H. Ozdener, V. Utermohlen, Identification of pro- and mature  
846 brain-derived neurotrophic factor in human saliva., *Archives of oral biology*  
847 54 (7) (2009) 689–695. doi:10.1016/j.archoralbio.2009.04.005.
- 848 [28] C. A. Schneider, W. S. Rasband, K. W. Eliceiri, NIH Image to ImageJ:  
849 25 years of image analysis, *Nature Methods* 9 (7) (2012) 671–675. arXiv:  
850 arXiv:1011.1669v3, doi:10.1038/nmeth.2089.
- 851 [29] R. W. Burry, Controls for immunocytochemistry: an update., *The journal*  
852 *of histochemistry and cytochemistry : official journal of the Histochemistry*  
853 *Society* 59 (1) (2011) 6–12. doi:10.1369/jhc.2010.956920.

- 854 [30] M. B. Mazalan, M. A. B. Ramlan, J. H. Shin, T. Ohashi, Effect of geomet-  
855 ric curvature on collective cell migration in tortuous microchannel devices,  
856 *Micromachines* 11 (7) (2020) 1–17. doi:[10.3390/MI11070659](https://doi.org/10.3390/MI11070659).
- 857 [31] F. Xu, T. Beyazoglu, E. Hefner, U. A. Gurkan, U. Demirci, Automated  
858 and adaptable quantification of cellular alignment from microscopic images  
859 for tissue engineering applications, *Tissue Engineering - Part C: Methods*  
860 17 (6) (2011) 641–649. doi:[10.1089/ten.tec.2011.0038](https://doi.org/10.1089/ten.tec.2011.0038).
- 861 [32] E. Batschelet, *Circular Statistics in Biology* (Mathematics in Biology Series),  
862 1st Edition, Academic Press, New York, NY, 1981.
- 863 [33] P. Berens, M. J. Velasco, CircStat for Matlab: Toolbox for circular statistics  
864 with Matlab, Max–Planck–Institut f ur biologische Kybernetik, Technical  
865 Report No. 184 31 (10) (2009) 1–21. doi:[doi:10.18637/jss.v031.i10](https://doi.org/10.18637/jss.v031.i10).
- 866 [34] M. Pool, J. Thiemann, A. Bar-Or, A. E. Fournier, NeuriteTracer: A novel  
867 ImageJ plugin for automated quantification of neurite outgrowth, *Journal*  
868 of Neuroscience Methods 168 (1) (2008) 134–139. doi:[10.1016/j.jneumeth.2007.08.029](https://doi.org/10.1016/j.jneumeth.2007.08.029).
- 869
- 870 [35] E. Meijering, M. Jacob, J.-C. F. Sarria, P. Steiner, H. Hirling, M. Unser,  
871 Design and validation of a tool for neurite tracing and analysis in fluo-  
872 rescence microscopy images., *Cytometry. Part A : the journal of the Inter-  
873 national Society for Analytical Cytology* 58 (2) (2004) 167–176. doi:  
874 [10.1002/cyto.a.20022](https://doi.org/10.1002/cyto.a.20022).
- 875 [36] M. Anniko, W. Arnold, T. Stigbrand, A. Strom, The Human Spiral Gan-  
876 glion, *ORL* 57 (1995) 68–77.
- 877 [37] S. van der Walt, S. C. Colbert, G. Varoquaux, The NumPy Array: A  
878 Structure for Efficient Numerical Computation, *Computing in Science En-  
879 gineering* 13 (2) (2011) 22–30. doi:[10.1109/MCSE.2011.37](https://doi.org/10.1109/MCSE.2011.37).
- 880 [38] J. D. Hunter, Matplotlib: A 2D Graphics Environment, *Computing in  
881 Science Engineering* 9 (3) (2007) 90–95. doi:[10.1109/MCSE.2007.55](https://doi.org/10.1109/MCSE.2007.55).

- 882 [39] P. Virtanen, R. Gommers, T. E. Oliphant, M. Haberland, T. Reddy,  
883 D. Cournapeau, E. Burovski, P. Peterson, W. Weckesser, J. Bright, S. J.  
884 van der Walt, M. Brett, J. Wilson, K. J. Millman, N. Mayorov, A. R. J.  
885 Nelson, E. Jones, R. Kern, E. Larson, C. J. Carey, I. Polat, Y. Feng,  
886 E. W. Moore, J. VanderPlas, D. Laxalde, J. Perktold, R. Cimrman, I. Hen-  
887 riksen, E. A. Quintero, C. R. Harris, A. M. Archibald, A. H. Ribeiro,  
888 F. Pedregosa, P. van Mulbregt, SciPy 1.0: fundamental algorithms for  
889 scientific computing in Python., *Nature methods* 17 (3) (2020) 261–272.  
890 doi:10.1038/s41592-019-0686-2.
- 891 [40] P. Berens, CircStat : A MATLAB Toolbox for Circular Statistics , *Journal*  
892 *of Statistical Software* 31 (10). doi:10.18637/jss.v031.i10.
- 893 [41] M. Tuncel, H. S. Sürkü, K. M. Erbil, A. Konan, Formation of the cochlear  
894 nerve in the modiolus of the guinea pig and human cochleae., *Archives of*  
895 *medical research* 36 (5) (2005) 436–40. doi:10.1016/j.arcmed.2005.02.  
896 003.
- 897 [42] B. Küçük, K. Abe, T. Ushiki, Y. Inuyama, S. Fukuda, Kazuo Ishikawa,  
898 Microstructures of the Bony Modiolus in the Human Cochlea : A Scanning  
899 Electron Microscopic Study, *Journal of Electron Microsc* 40 (40) (1991)  
900 193–197.
- 901 [43] O. Levenspiel, *Chemical Reaction Engineering*, 3rd Edition, John Wiley  
902 and Sons, Inc., New York, NY, 1999.
- 903 [44] M. Stroh, W. R. Zipfel, R. M. Williams, S. C. Ma, W. W. Webb, W. M.  
904 Saltzman, Multiphoton microscopy guides neurotrophin modification with  
905 poly(ethylene glycol) to enhance interstitial diffusion, *Nature Materials*  
906 3 (7) (2004) 489–494. doi:10.1038/nmat1159.
- 907 [45] S. Axler, *Linear Algebra Done Right*, 3rd Edition, Springer Publishing,  
908 New York, NY, 2015.

- 909 [46] J. Crank, The mathematics of Diffusion, 2nd Edition, Oxford University  
910 Press, London, UK, 1979.
- 911 [47] K. M. Keefe, I. S. Sheikh, G. M. Smith, Targeting Neurotrophins to Specific  
912 Populations of Neurons: NGF, BDNF, and NT-3 and Their Relevance  
913 for Treatment of Spinal Cord Injury., International journal of molecular  
914 sciences 18 (3). doi:10.3390/ijms18030548.
- 915 [48] B. I. Awad, M. A. Carmody, M. P. Steinmetz, Potential role of growth  
916 factors in the management of spinal cord injury., World Neurosurgery 83 (1)  
917 (2015) 120–131. doi:10.1016/j.wneu.2013.01.042.
- 918 [49] E. R. n. Hollis, M. H. Tuszynski, Neurotrophins: potential therapeutic tools  
919 for the treatment of spinal cord injury., Neurotherapeutics : the journal of  
920 the American Society for Experimental NeuroTherapeutics 8 (4) (2011)  
921 694–703. doi:10.1007/s13311-011-0074-9.
- 922 [50] A. H. Nagahara, B. R. Wilson, I. Ivasyk, I. Kovacs, S. Rawalji, J. R.  
923 Bringas, P. J. Piviroto, W. S. Sebastian, L. Samaranch, K. S. Bankiewicz,  
924 M. H. Tuszynski, MR-guided delivery of AAV2-BDNF into the entorhi-  
925 nal cortex of non-human primates., Gene therapy 25 (2) (2018) 104–114.  
926 doi:10.1038/s41434-018-0010-2.
- 927 [51] S. D. Croll, C. Suri, D. L. Compton, M. V. Simmons, G. D. Yan-  
928 copoulos, R. M. Lindsay, S. J. Wiegand, J. S. Rudge, H. E. Scharfman,  
929 Brain-derived neurotrophic factor transgenic mice exhibit passive avoid-  
930 ance deficits, increased seizure severity and in vitro hyperexcitability in  
931 the hippocampus and entorhinal cortex., Neuroscience 93 (4) (1999) 1491–  
932 1506. doi:10.1016/s0306-4522(99)00296-1.
- 933 [52] A. Dravid, S. Parittotokkaporn, Z. Aqrawe, S. J. O'Carroll, D. Svirskis,  
934 Determining Neurotrophin Gradients in Vitro to Direct Axonal Outgrowth  
935 following Spinal Cord Injury, ACS Chemical Neuroscience 11 (2) (2020)  
936 121–132. doi:10.1021/acschemneuro.9b00565.

- 937 [53] T. Yamagata, J. M. Miller, M. Ulfendahl, N. P. Olivius, R. A. Altschuler,  
938 I. Pyykkö, G. Bredberg, Delayed neurotrophic treatment preserves nerve  
939 survival and electrophysiological responsiveness in neomycin-deafened  
940 guinea pigs., *Journal of neuroscience research* 78 (1) (2004) 75–86. doi:  
941 10.1002/jnr.20239.
- 942 [54] M. P. Zanin, M. Hellstr??m, R. K. Shepherd, A. R. Harvey, L. N. Gillespie,  
943 Development of a cell-based treatment for long-term neurotrophin expres-  
944 sion and spiral ganglion neuron survival, *Neuroscience* 277 (2014) 690–699.  
945 doi:10.1016/j.neuroscience.2014.07.044.
- 946 [55] M. Seyyedi, L. Viana, J. J. Nadol, Within-subject comparison of word  
947 recognition and spiral ganglion cell count in bilateral cochlear implant  
948 recipients, *Otol Neurotol* 35 (8) (2014) 1446–1450. doi:10.1097/MAO.  
949 000000000000443.Within-Subject.
- 950 [56] A. Henriques, C. Pitzer, A. Schneider, Neurotrophic growth factors for the  
951 treatment of amyotrophic lateral sclerosis: where do we stand?, *Frontiers*  
952 in neuroscience
- 4 (2010) 32. doi:10.3389/fnins.2010.00032.
- 953 [57] J. F. Poduslo, G. L. Curran, Permeability at the blood-brain and  
954 blood-nerve barriers of the neurotrophic factors: NGF, CNTF, NT-3,  
955 BDNF, *Molecular Brain Research* 36 (2) (1996) 280–286. doi:10.1016/  
956 0169-328X(95)00250-V.
- 957 [58] T. Sakane, W. M. Pardridge, Carboxyl-directed pegylation of brain-derived  
958 neurotrophic factor markedly reduces systemic clearance with minimal loss  
959 of biologic activity (1997). doi:10.1023/A:1012117815460.
- 960 [59] R. G. Soderquist, E. D. Milligan, E. M. Sloane, J. A. Harrison, K. K.  
961 Douvas, J. M. Potter, T. S. Hughes, R. A. Chavez, K. Johnson, L. R.  
962 Watkins, M. J. Mahoney, PEGylation of brain-derived neurotrophic factor  
963 for preserved biological activity and enhanced spinal cord distribution.,  
964 *Journal of biomedical materials research. Part A* 91 (3) (2009) 719–729.  
965 doi:10.1002/jbm.a.32254.

- 966 [60] M. Sasi, B. Vignoli, M. Canossa, R. Blum, Neurobiology of local and inter-  
967 cellular BDNF signaling, *Pflugers Archiv : European journal of physiology*  
968 469 (5-6) (2017) 593–610. doi:10.1007/s00424-017-1964-4.
- 969 [61] X. Li, Y. Su, S. Liu, L. Tan, X. Mo, S. Ramakrishna, Encapsulation  
970 of proteins in poly(l-lactide-co-caprolactone) fibers by emulsion electro-  
971 spinning, *Colloids and Surfaces B: Biointerfaces* 75 (2) (2010) 418–424.  
972 doi:10.1016/j.colsurfb.2009.09.014.
- 973 [62] E. E. L. Swan, M. Peppi, Z. Chen, K. M. Green, J. E. Evans, M. J.  
974 McKenna, M. J. Mescher, S. G. Kujawa, W. F. Sewell, Proteomics analysis  
975 of perilymph and cerebrospinal fluid in mouse., *The Laryngoscope* 119 (5)  
976 (2009) 953–958. doi:10.1002/lary.20209.
- 977 [63] T. Numakawa, S. Suzuki, E. Kumamaru, N. Adachi, M. Richards,  
978 H. Kunugi, BDNF function and intracellular signaling in neurons, *Histology  
and Histopathology* 25 (2) (2010) 237–258. doi:10.14670/HH-25.237.
- 980 [64] C. Gentile, Engineering of Spheroids for Stem Cell Technology, *Current  
981 Stem Cell Research & Therapy* 11 (2016) 652–665. doi:10.2174/  
982 1574888x10666151001114848.
- 983 [65] H. Berg, *Random Walks in Biology*, Princeton Universtiyy Press, Prinston,  
984 NJ, 1983.
- 985 [66] H. Li, F. Edin, H. Hayashi, O. Gudjonsson, N. Danckwardt-Lillies, H. En-  
986 gqvist, H. Rask-Andersen, W. Xia, Guided growth of auditory neurons:  
987 Bioactive particles towards gapless neural electrode interface, *Biomaterials*  
988 122 (2017) 1–9. doi:10.1016/j.biomaterials.2016.12.020.
- 989 [67] J. Schulze, H. Staeker, D. Wedekind, T. Lenarz, A. Warnecke, Expression  
990 pattern of brain-derived neurotrophic factor and its associated receptors:  
991 Implications for exogenous neurotrophin application., *Hearing Research* 413  
992 (2020) 108098. doi:10.1016/j.heares.2020.108098.